SCIENCE CHINA
Information Sciences

• RESEARCH PAPER •

August 2026, Vol. 69, Iss. 8, 182202:1–182202:23
https://doi.org/10.1007/s11432-025-4977-0

Fast and high-precision estimation of phase and Doppler frequency for X-ray pulsar-based navigation based on prior information and non-convex optimization

Wenjia ZHANG[1,2], Xin MA[1,2*], Peiling CUI[1,2], Xiaolin NING[1,2,3], Weiren WU[4] & Jiancheng FANG[1,2]

[1]*School of Instrumentation Science and Opto-Electronics Engineering, Beihang University, Beijing 100191, China*
[2]*Institute of Large-scale Scientific Facility, Beihang University, Beijing 100191, China*
[3]*Hefei National Laboratory, Hefei 230088, China*
[4]*Lunar Exploration and Space Program Center, China National Space Administration, Beijing 100037, China*

Received 13 October 2025/Revised 11 January 2026/Accepted 10 February 2026/Published online 31 July 2026

Abstract In X-ray pulsar-based navigation, phase and Doppler frequency estimation based on the maximum likelihood estimation and grid search methods is widely used in practical missions and theoretical analysis. However, due to the non-convexity of the objective function and the inefficiency of the grid search method, a key challenge is how to achieve fast estimation of phase and Doppler frequency while maintaining accuracy. To address this issue, the fast and high-precision estimation of phase and Doppler frequency based on prior information and non-convex optimization is proposed in this paper. First, leveraging the prior state information of the spacecraft, an enhanced on-orbit phase model is established by considering a reference time at any given moment. Then, the statistical properties of the parameters to be estimated are analyzed, and the corresponding prior probability model is constructed, using the Bayesian estimation model as the objective function. Finally, incorporating non-convex optimization theory, the Nesterov-adaptive moment estimation is employed to automatically adjust the step size of the quasi-Newton algorithm. Simulation and experimental results demonstrate that the proposed method achieves rapid convergence with high precision, effectively balancing real-time performance and estimation accuracy compared to traditional phase and Doppler frequency estimation methods. Using the Crab pulsar as the primary case study, when the observation duration is 1800 s and the detector area is 30 cm^2, the proposed method reduces the running time by 99.91% and 73.68% compared to the traditional grid search and adaptive grid search methods, respectively. Moreover, the proposed method yields positioning errors below 10 km under rapid estimation conditions.

Keywords X-ray pulsar-based navigation, phase estimation, Doppler frequency estimation, Bayesian estimation

Citation Zhang W J, Ma X, Cui P L, et al. Fast and high-precision estimation of phase and Doppler frequency for X-ray pulsar-based navigation based on prior information and non-convex optimization. Sci China Inf Sci, 2026, 69(8): 182202, https://doi.org/10.1007/s11432-025-4977-0

1 Introduction

As humanity advances in space exploration, autonomous navigation for spacecraft has become increasingly important. The traditional celestial navigation system (CNS) has been implemented in various space missions [1], but its navigation performance will decline due to the impact of the complex space environment. X-ray pulsar-based navigation (XNAV) is a highly promising autonomous navigation method that can be applied throughout space [2–5]. The European Space Agency (ESA) conducted a feasibility study on utilizing pulsar timing information for spacecraft navigation in 2004 [6]. The launch of the Neutron Star Interior Composition Explorer (NICER) mission in 2017 has provided valuable data for XNAV research [7, 8]. In 2016, China successfully launched the X-ray pulsar navigation experimental satellite (XPNAV-1) [9]. Subsequently, POLAR [10] and the Insight-HXMT satellite [11] were utilized to process X-ray pulsar data and validate XNAV.

In XNAV, an onboard detector records the time-of-arrival (TOA) of X-ray photons. By processing these photon arrival times, the pulse phase can be estimated, which in turn enables the determination of pulse time delay [12–14]. Once the pulse time delay is obtained, the spacecraft's state information can be derived. Therefore, pulse phase estimation is of critical importance. Pulse phase estimation refers to estimating the phase at either the initial time t_0 or the final time t_f within an observation interval $[t_0, t_f)$. Estimating the phase at t_0 is the fundamental

* Corresponding author (email: maxin@buaa.edu.cn)

phase estimation task, also known as initial phase estimation [15]. Unless otherwise specified, the phase estimation mentioned in this paper refers to initial phase estimation. Although pulsar phase measurements can infer spacecraft states, the solvability of observation equations in pulsar-based navigation also depends on geometry. Similar to the singular positioning problem described by Liu et al. [16], near-coplanar pulsar distributions or third-body obstructions may render the observation matrix rank-deficient, causing local instability or blind zones. To prevent this, geometric observability constraints (e.g., weighted dilution of precision, WDOP [17]) are applied during pulsar selection to maintain a well-conditioned geometry. This work therefore focuses on phase and Doppler frequency estimation, assuming that suitable pulsar geometry has been ensured.

During spacecraft flight, its velocity continuously changes, making the estimation of phase and Doppler frequency challenging due to the influence of Doppler effects. Currently, this issue is mainly addressed using phase tracking methods [18–21] and estimation methods based on on-orbit phase model [22–25]. The phase tracking method divides an observation period into multiple sub-observation periods, which reduces estimation accuracy. In contrast, the estimation method based on the on-orbit phase model mitigates the impact of Doppler frequency by considering the spacecraft's motion state and has been widely studied.

After establishing the on-orbit phase model, epoch folding (EF) [23] and maximum likelihood estimation (MLE) [22, 24, 25] methods are commonly used to obtain phase and Doppler frequency. Compared to the EF method, the MLE method can achieve the Cramér-Rao lower bound (CRLB). However, the likelihood function (LF) used in MLE is a non-convex function with multiple local maxima, leading to the widespread study and application of the two-dimensional grid search method. Nevertheless, the estimation accuracy and efficiency of the grid search method depend on the grid size and search interval, making it challenging to achieve both high accuracy and high efficiency simultaneously. To address the challenge, Xue et al. [26] first used the H-test to estimate the Doppler frequency, and then used fast MLE to estimate the phase. Although it provides higher efficiency, it sacrifices some accuracy. Wang et al. [24] proposed X-ray pulsar-based navigation using on-orbit pulsar timing (XTITAN). However, XTITAN divides an observation period into several sub-observation periods to enable iterative estimation, which can decrease estimation accuracy. Some researchers have attempted to narrow the search range for phase and Doppler frequency by calculating the bounds of phase estimation error and Doppler frequency estimation error [22, 25, 27]. On the basis of Su et al. [27], Wang et al. [25] proposed an adaptive grid search (AGS) method in 2024. However, this method still relies on two-dimensional grid search for phase and Doppler frequency, where the computational complexity depends on the search interval. Especially when the prior information is inaccurate, the estimation efficiency of AGS is very low. Therefore, narrowing the estimation range to improve computational efficiency is limited, as it does not change the estimation accuracy. The reason for using grid search to solve MLE is that the LF is a non-convex function, and there is currently no efficient, high-precision non-convex optimization algorithm that effectively addresses this problem [15, 28]. In recent years, although a few researchers have attempted to use optimization methods or intelligent algorithms for phase and Doppler frequency estimation, such as Nelder-Mead simplex algorithm [29], adaptive moment estimation (Adam) [30], and Newton-Raphson method [31], they cannot guarantee obtaining the optimal estimates. This is because the objective function remains non-convex over a large search space, essentially treating a non-convex optimization problem with convex optimization techniques. This highlights the infeasibility of solely relying on simple convex optimization methods.

Based on the above analysis, current estimation methods primarily rely on two-dimensional grid search to solve the objective function established using the on-orbit phase model and likelihood function. However, this approach fails to achieve both high accuracy and computational efficiency simultaneously. The estimation of phase and Doppler frequency remains an open challenge. To address this issue, the fast and high-precision phase and Doppler frequency estimation (FHPDE) method is proposed. Compared to the two-dimensional grid search method, FHPDE reduces the parameter search space and achieves rapid convergence within the search region without the need to compute the objective function value point by point, thereby balancing both efficiency and accuracy. The main contributions of this paper are as follows.

(1) The proposed enhanced on-orbit phase and Doppler frequency estimation method allows the use of an arbitrary reference time while preserving the accuracy of the pulsar's spin frequency. Additionally, prior information on phase and Doppler frequency can be derived from the spacecraft's prior state errors.

(2) Based on the prior information of phase and Doppler frequency, a general Bayesian risk function is constructed based on the Bayesian model and a loss function. By selecting different loss functions, different objective functions can be obtained.

(3) A fast and high-precision non-convex optimization method with interval constraints is proposed. This method efficiently determines an appropriate step size and imposes boundary constraints on unknown parameters, achieving a balance between estimation accuracy and real-time performance.

To provide a clearer overview of the proposed method and the logical relationships among its components, the

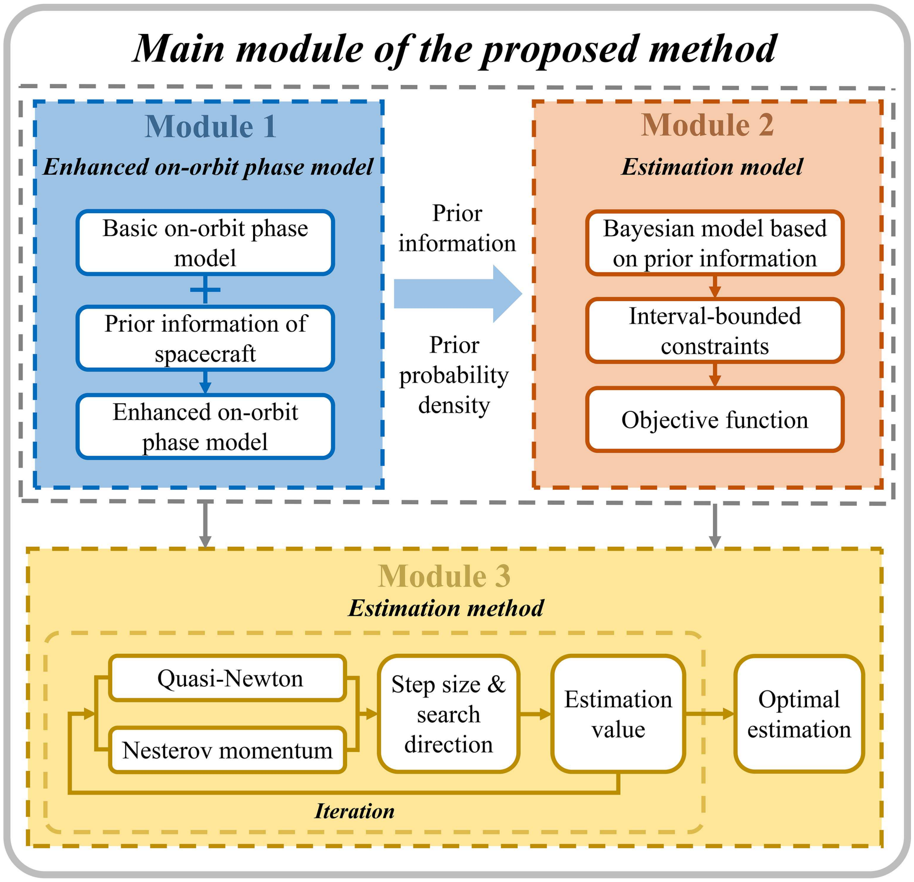

Figure 1 (Color online) Main modules of the proposed method.

overall framework of the FHPDE method is illustrated in Figure 1. The framework consists of three main modules: Module 1 establishes an enhanced on-orbit phase model by incorporating prior spacecraft information; Module 2 constructs a Bayesian-based estimation model with interval-bounded constraints to formulate the objective function; and Module 3 develops an efficient estimation method that adopts quasi-Newton optimization with Nesterov momentum to obtain the optimal estimation results. This modular structure systematically reflects the logical framework of the proposed method, where Section 2 corresponds to Module 1, and Section 3 includes Modules 2 and 3.

2 Enhanced on-orbit phase model and its prior information

2.1 Basic on-orbit phase propagation model

In X-ray pulsar navigation, a spacecraft detects X-ray pulsar signals using an onboard detector. During the j-th observation period, the arrival times of N pulsar photons detected at the spacecraft are denoted as $\{t_{i,\mathrm{sc}}^j\}_{i=0}^N$. Given the immense distance from the pulsars to the solar system barycenter (SSB), their proper motion can be neglected. Consequently, as shown in Figure 2, the distance between a pulsar and the spacecraft at time $t_{i,\mathrm{sc}}^j$ can be expressed as

$$\boldsymbol{d}_i^j = \boldsymbol{r}_i^j - \boldsymbol{D}, \quad d_i^j = |\boldsymbol{r}_i^j - \boldsymbol{D}| \approx \boldsymbol{n} \cdot (\boldsymbol{r}_i^j - \boldsymbol{D}), \tag{1}$$

where $\boldsymbol{r}_i^j$ represents the spacecraft's position vector relative to the SSB at the time $t_{i,\mathrm{sc}}^j$, $\boldsymbol{D}$ is the direction vector from the SSB to the observed pulsar, and $\boldsymbol{n}$ represents the unit direction vector from the SSB to the target pulsar. $\boldsymbol{d}_i^j$ represents the direction from the pulsar to the spacecraft, and $d_i^j = |\boldsymbol{d}_i^j|$ denotes its magnitude, where the operator $|\cdot|$ calculates the Euclidean norm of a vector.

Considering the spacecraft's motion, the basic on-orbit phase propagation model can be expressed as [23]

$$\phi_i^j = \phi_0^j + f_s(t_{i,\mathrm{sc}}^j - t_{0,\mathrm{sc}}^j) + \frac{f_s}{c}\boldsymbol{n} \cdot (\boldsymbol{r}_i^j - \boldsymbol{r}_0^j), \tag{2}$$

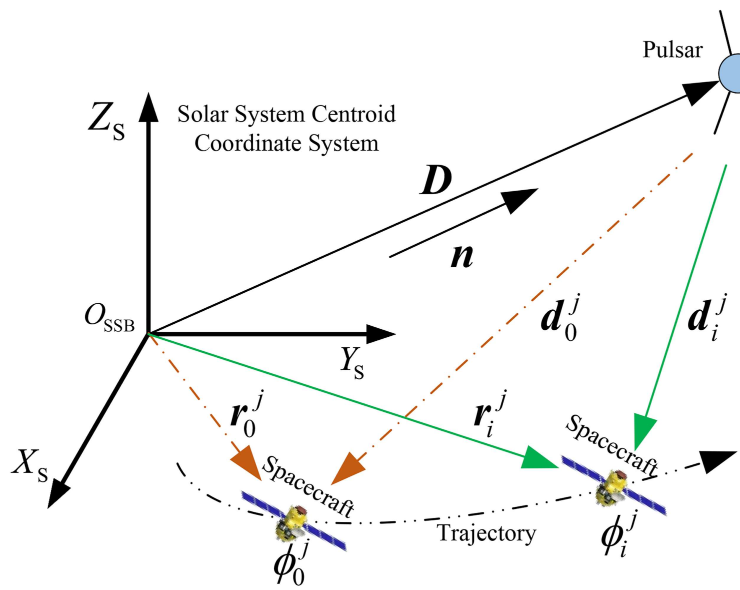

Figure 2 (Color online) Scenario diagram of XNAV and phase propagation (during the j-th observation period).

where ϕ_i^j represents the pulse phase at the time $t_{i,\mathrm{sc}}^j$, and ϕ_0^j is the pulse initial phase at the time $t_{0,\mathrm{sc}}^j$. f_s is the source frequency of pulsar, c is the speed of light.

2.2 Establishment of the enhanced on-orbit phase model

Based on (2), Wang et al. [24,25] established an on-orbit phase model by fixing the reference time at the beginning of the observation period while neglecting the accuracy of the pulsar's spin frequency. Therefore, this subsection considers an arbitrary reference time while preserving the accuracy of the pulsar's spin frequency to develop a more general on-orbit phase model. At the end of this subsection, the on-orbit phase model is linked to the spacecraft's prior state errors to obtain prior information on phase and Doppler frequency.

To estimate parameters such as pulse phase and Doppler frequency, a time transformation model is required to convert $\{t_{i,\mathrm{sc}}^j\}_{i=0}^N$ into the SSB time frame, denoted as $\{t_{i,\mathrm{ssb}}^j\}_{i=0}^N$. The time transformation model for the arrival time of the i-th photon in the j-th observation period can be expressed as [12]

$$t_{i,\mathrm{ssb}}^j = g(t_{i,\mathrm{sc}}^j) = t_{i,\mathrm{sc}}^j + \frac{1}{c}\boldsymbol{n}^{\mathrm{T}} \cdot \boldsymbol{r}_i^j + \mathrm{H.O.T}, \tag{3}$$

where the function $g(\cdot)$ represents the time conversion function. H.O.T represents the higher-order terms accounting for relativistic time delay effects, which can be expressed as

$$\mathrm{H.O.T} = \frac{1}{2cD}\left[-\|\boldsymbol{r}_i^j\| + (\boldsymbol{n}^{\mathrm{T}} \cdot \boldsymbol{r}_i^j)^2 + 2(\boldsymbol{n}^{\mathrm{T}} \cdot \boldsymbol{b})(\boldsymbol{n}^{\mathrm{T}} \cdot \boldsymbol{r}) - 2(\boldsymbol{b} \cdot \boldsymbol{r})\right] + \frac{2\mu_{\mathrm{s}}}{c^3} \ln\left|\frac{\boldsymbol{n}^{\mathrm{T}} \cdot (\boldsymbol{r}_i^j + \boldsymbol{b}) + \|\boldsymbol{r}_i^j + \boldsymbol{b}\|}{\boldsymbol{n}^{\mathrm{T}} \cdot \boldsymbol{b} + \|\boldsymbol{b}\|}\right|, \tag{4}$$

where $\boldsymbol{b}$ denotes the direction vector from the SSB to the Sun, and D is the distance from the observed pulsar to the SSB.

Assuming that the pulse phase at the reference time T_0 is ϕ_{T_0}, the pulse phase model at any time $t_{i,\mathrm{sc}}^j$ is given by

$$\phi_i^j = \phi_{T_0} + f_0\left[g(t_{i,\mathrm{sc}}^j) - T_0\right] + \frac{f_1}{2}\left[g(t_{i,\mathrm{sc}}^j) - T_0\right]^2, \tag{5}$$

where f_0 and f_1 are the pulsar's spin frequency and its first derivative at the reference time T_0. Therefore, the pulse initial phase ϕ_0^j at $t_{0,\mathrm{sc}}^j$ can be expressed as

$$\phi_0^j = \phi_{T_0} + f_0\left[g(t_{0,\mathrm{sc}}^j) - T_0\right] + \frac{f_1}{2}\left[g(t_{0,\mathrm{sc}}^j) - T_0\right]^2. \tag{6}$$

By subtracting (6) from (5), we get

$$\phi_i^j = \phi_0^j + f_0\left[g(t_{i,\mathrm{sc}}^j) - g(t_{0,\mathrm{sc}}^j)\right] + \frac{f_1}{2}\left\{\left[g(t_{i,\mathrm{sc}}^j) - T_0\right]^2 - \left[g(t_{0,\mathrm{sc}}^j) - T_0\right]^2\right\}. \tag{7}$$

According to (3) and (4), the pulse phase model in (7) is determined by the spacecraft's position. However, in practical navigation scenarios, the true position of the spacecraft is unknown. To account for the impact of spacecraft state estimation errors on the phase model (7), we define $\{\boldsymbol{r}_i^j\}_{i=0}^N$ and $\{\boldsymbol{v}_i^j\}_{i=0}^N$ as the true position and velocity of the spacecraft at times $\{t_{i,\mathrm{sc}}^j\}_{i=0}^N$, respectively. Similarly, we define $\{\hat{\boldsymbol{r}}_i^j\}_{i=0}^N$ and $\{\hat{\boldsymbol{v}}_i^j\}_{i=0}^N$ as the estimated position and velocity of the spacecraft at the corresponding times.

By performing a Taylor series expansion of (7) at any estimated position $\hat{\boldsymbol{r}}_i^j$ and initial estimated position $\hat{\boldsymbol{r}}_0^j$, ϕ_i^j can be expressed as (with detailed derivation provided in Appendix A)

$$\phi_i^j = \phi_0^j + \hat{\phi}_i^j + \left\{ f_0 + f_1 \left[g(\hat{t}_{i,\mathrm{sc}}^j) - T_0 \right] \right\} \cdot \left(\boldsymbol{G}_i \Delta \boldsymbol{r}_i^j - \boldsymbol{G}_0 \Delta \boldsymbol{r}_0^j \right), \tag{8}$$

where $\Delta\boldsymbol{r}_i^j$ and $\Delta\boldsymbol{r}_0^j$ represent the estimation errors of the spacecraft's position, and $\boldsymbol{G}_i$ and $\boldsymbol{G}_0$ denote the partial derivatives of (3) with respect to the spacecraft position, given by

$$\boldsymbol{G}_i = \left. \frac{\partial g(t_{i,\mathrm{sc}}^j)}{\partial \boldsymbol{r}_i^j} \right|_{\boldsymbol{r}_i^j = \hat{\boldsymbol{r}}_i^j}, \quad \boldsymbol{G}_0 = \left. \frac{\partial g(t_{0,\mathrm{sc}}^j)}{\partial \boldsymbol{r}_0^j} \right|_{\boldsymbol{r}_0^j = \hat{\boldsymbol{r}}_0^j}. \tag{9}$$

The term $\hat{\phi}_i^j$ represents the phase deviation caused by time variation, expressed as

$$\hat{\phi}_i^j = f_0 \left[g(\hat{t}_{i,\mathrm{sc}}^j) - g(\hat{t}_{0,\mathrm{sc}}^j) \right] + \frac{f_1}{2} \left\{ \left[g(\hat{t}_{i,\mathrm{sc}}^j) - T_0 \right]^2 - \left[g(\hat{t}_{0,\mathrm{sc}}^j) - T_0 \right]^2 \right\}. \tag{10}$$

Although Eq. (8) incorporates the prior information on the spacecraft state, it is still necessary to establish a transformation model between the initial phase to be estimated, ϕ_0^j, and the prior state information. By performing a Taylor series expansion of (6) at the initial estimated position $\hat{\boldsymbol{r}}_0^j$, ϕ_0^j can be expressed as

$$\phi_0^j = \phi_{T_0} + f_0 \cdot \left[g(\hat{t}_{0,\mathrm{sc}}^j) - T_0 \right] + f_0 \boldsymbol{G}_0 \cdot \Delta \boldsymbol{r}_0^j. \tag{11}$$

In deriving (11) from (6), the quadratic term $[g(t_{0,\mathrm{sc}}^j) - T_0]^2$ has been omitted. This omission is justified as follows. On the one hand, compared to f_0, the value of f_1 is significantly smaller. For instance, when the reference time T_0 is March 9, 2020 (MJD = 58917), the Crab pulsar has a spin frequency of $f_0 = 29.6096$ Hz, whereas f_1 is only $-368174.57 \times 10^{-15}\ \mathrm{s}^{-2}$. On the other hand, Jodrell Bank Centre for Astrophysics publishes ephemeris information for the Crab pulsar every month, allowing the reference time T_0 to be conveniently selected as the time closest to the mission start. This ensures that $g(t_{0,\mathrm{sc}}^j) - T_0$ is theoretically less than 30 days. Thus, the quadratic term can be safely neglected when computing (11).

In (11), let $\tilde{\phi}_0^j = \phi_{T_0} + f_0 \cdot [g(\hat{t}_{0,\mathrm{sc}}^j) - T_0]$ and $\Delta\phi_0^j = f_0 \boldsymbol{G}_0 \cdot \Delta\boldsymbol{r}_0^j$, yielding

$$\phi_0^j = \tilde{\phi}_0^j + \Delta\phi_0^j. \tag{12}$$

Substituting (12) into (8), the enhanced on-orbit phase propagation model incorporating prior information on the spacecraft state can be expressed as

$$\phi_i^j = \tilde{\phi}_0^j + \Delta\phi_0^j + \hat{\phi}_i^j + \left\{ f_0 + f_1 \cdot \left[g(\hat{t}_{i,\mathrm{sc}}^j) - T_0 \right] \right\} \cdot \left(\boldsymbol{G}_i \Delta \boldsymbol{r}_i^j - \boldsymbol{G}_0 \Delta \boldsymbol{r}_0^j \right). \tag{13}$$

Refs. [24, 25] have established phase propagation models similar to (8) and (13). However, the on-orbit phase propagation model proposed in this paper is more general and rigorous. First, the reference time T_0 in this work can be arbitrarily chosen, whereas in [24,25], the reference time is fixed at the start of an observation period, i.e., $g(t_{0,\mathrm{sc}}^j)$. Second, Ref. [24] did not establish a relationship between the initial phase and prior spacecraft state information. Although Ref. [25] considered the effect of prior spacecraft information on the initial phase, it compromised the precision of the pulsar spin frequency. Moreover, the frequency information at $g(t_{0,\mathrm{sc}}^j)$ used in [25] is not readily accessible. The enhanced on-orbit phase propagation model proposed in this paper elegantly resolves these issues. Theoretically, T_0 can be chosen arbitrarily. However, we recommend setting T_0 to match the epoch of the pulsar ephemeris data published by the Jodrell Bank Centre for Astrophysics, which facilitates the precise configuration of pulsar frequency parameters. For example, if the mission or observation period starts on March 25, 2024, and the target pulsar is Crab, then according to the Crab ephemeris published by the Jodrell Bank Centre for Astrophysics[1)],

1) https://www.jb.man.ac.uk/pulsar/crab/crab2.txt.

the reference time T_0 can be set to March 15, 2024. At this epoch, the spin frequency f_0 is 29.5630 Hz, and the frequency derivative f_1 is -366709.10×10^{-15} s^{-2}.

According to the properties of the orbital dynamics model, the spacecraft position error is related to the initial position and velocity errors and can be expressed as

$$\Delta \boldsymbol{r}_i^j = \boldsymbol{\Phi}_{\mathrm{rr}}(t_{i,\mathrm{sc}}^j, t_{0,\mathrm{sc}}^j)\Delta \boldsymbol{r}_0^j + \boldsymbol{\Phi}_{\mathrm{rv}}(t_{i,\mathrm{sc}}^j, t_{0,\mathrm{sc}}^j)\Delta \boldsymbol{v}_0^j, \tag{14}$$

where $\boldsymbol{\Phi}_{\mathrm{rr}}(t_{i,\mathrm{sc}}^j, t_{0,\mathrm{sc}}^j)$ and $\boldsymbol{\Phi}_{\mathrm{rv}}(t_{i,\mathrm{sc}}^j, t_{0,\mathrm{sc}}^j)$ are state transition matrices, which can be represented as

$$\begin{cases} \boldsymbol{\Phi}_{\mathrm{rr}}(t_{i,\mathrm{sc}}^j, t_{0,\mathrm{sc}}^j) = \boldsymbol{I}_{3\times3} + \displaystyle\sum_{m=1}^{+\infty} \frac{1}{m!}\boldsymbol{\varphi}_m (t_{i,\mathrm{sc}}^j - t_{0,\mathrm{sc}}^j)^m, \\ \boldsymbol{\Phi}_{\mathrm{rv}}(t_{i,\mathrm{sc}}^j, t_{0,\mathrm{sc}}^j) = \displaystyle\sum_{m=1}^{+\infty} \frac{1}{m!}\boldsymbol{\gamma}_m (t_{i,\mathrm{sc}}^j - t_{0,\mathrm{sc}}^j)^m, \end{cases} \tag{15}$$

where $\boldsymbol{\varphi}_m$ and $\boldsymbol{\gamma}_m$ are constant matrices. Ref. [24] has demonstrated that the value of m is related to the observation duration and the altitude of the spacecraft. For NICER observation data, m can be set to 1. Therefore, for convenience and without loss of generality, we set $m = 1$. Substituting (14) and (15) into (13), we obtain

$$\begin{aligned} \phi_i^j =& \tilde{\phi}_0^j + \Delta\phi_0^j + \hat{\phi}_i^j + \left\{ f_0 + f_1 \cdot \left[g(\hat{t}_{i,\mathrm{sc}}^j) - T_0 \right] \right\} \cdot \boldsymbol{G}_i \left[\boldsymbol{I}_{3\times3} + \boldsymbol{\varphi}_1 (t_{i,\mathrm{sc}}^j - t_{0,\mathrm{sc}}^j) \right] \Delta \boldsymbol{r}_0^j \\ &+ \left\{ f_0 + f_1 \left[g(\hat{t}_{i,\mathrm{sc}}^j) - T_0 \right] \right\} \boldsymbol{G}_i \boldsymbol{\gamma}_1 (t_{i,\mathrm{sc}}^j - t_{0,\mathrm{sc}}^j) \Delta \boldsymbol{v}_0^j - \left\{ f_0 + f_1 \left[g(\hat{t}_{i,\mathrm{sc}}^j) - T_0 \right] \right\} \boldsymbol{G}_0 \Delta \boldsymbol{r}_0^j. \end{aligned} \tag{16}$$

Since, over an observation period (typically a few hundred to a few thousand seconds), celestial bodies such as the Sun, Mars, Jupiter, and Earth can be considered stable, we approximate $\boldsymbol{G}_i \approx \boldsymbol{G}_0$. Thus, the on-orbit phase propagation model considering the prior state information of the spacecraft can be expressed as

$$\phi_i^j = \tilde{\phi}_0^j + \Delta\phi_0^j + \hat{\phi}_i^j + f_{\mathrm{d}}(t_{i,\mathrm{sc}}^j - t_{0,\mathrm{sc}}^j), \tag{17}$$

where f_{d} is given by

$$f_{\mathrm{d}} = \left\{ f_0 + f_1 \left[g(\hat{t}_{i,\mathrm{sc}}^j) - T_0 \right] \right\} \left(\boldsymbol{G}_i \boldsymbol{\varphi}_1 \Delta \boldsymbol{r}_0^j + \boldsymbol{G}_i \boldsymbol{\gamma}_1 \Delta \boldsymbol{v}_0^j \right). \tag{18}$$

2.3 Prior probability density of phase and Doppler frequency

Before establishing the prior probability models for phase and Doppler frequency, this subsection briefly explains the physical process of obtaining the prior information. In practical pulsar-based navigation, the estimation of phase and Doppler frequency is usually performed once every K observation periods, where K represents the interval between two estimation epochs. The value of K depends on navigation accuracy, spacecraft dynamics, signal-to-noise ratio (SNR), and computational cost. A smaller K provides more frequent updates but increases the processing load, while a larger K reduces computation but leads to greater prior uncertainty due to longer propagation.

As illustrated in Figure 3, during the $(j-K)$-th observation period, the Kalman filtering provides the spacecraft state covariance $\boldsymbol{P}_{j-K}$, which characterizes the statistical uncertainty of the position and velocity estimates. Since the true state errors are not directly measurable, their uncertainty is propagated statistically rather than deterministically, following

$$\boldsymbol{P}_{j|j-K} = \mathbf{\Phi}_{j,j-K}\, \boldsymbol{P}_{j-K}\, \mathbf{\Phi}_{j,j-K}^{\mathrm{T}} + \boldsymbol{Q}_{j,j-K}, \tag{19}$$

where $\mathbf{\Phi}_{j,j-K}$ is the state transition matrix and $\boldsymbol{Q}_{j,j-K}$ is the process noise covariance. The propagated covariance $\boldsymbol{P}_{j|j-K}$ thus serves as the prior statistical basis for the j-th estimation epoch. Its position and velocity components ($\boldsymbol{P}_{\mathrm{r}}$ and $\boldsymbol{P}_{\mathrm{v}}$) determine the variances of the prior phase and Doppler frequency distributions.

Based on the Kalman filtering, the propagated covariance $\boldsymbol{P}_{j|j-K}$, the position and velocity estimation errors $\Delta \boldsymbol{r}_0^j$ and $\Delta \boldsymbol{v}_0^j$ are modeled as zero-mean Gaussian random variables with variances determined by $\boldsymbol{P}_{j|j-K}$. Accordingly, the prior phase estimation error $\Delta\phi_0^j$ and Doppler frequency estimation error f_{d} also follow zero-mean Gaussian distributions due to the linear relationship between the measurement model and the state estimation errors. Thus, based on (12) and (18), both ϕ_0^j and f_{d} also follow a normal distribution.

The mean and variance of ϕ_0^j are given by

$$\begin{cases} m_{\phi_0} = \mathrm{E}(\tilde{\phi}_0^j + \Delta\phi_0^j) = \tilde{\phi}_0^j, \\ \sigma_{\phi_0}^2 = \mathrm{Var}(\tilde{\phi}_0^j + \Delta\phi_0^j) = f_0^2 \boldsymbol{G}_0 \boldsymbol{P}_{\mathrm{r}} \boldsymbol{G}_0^{\mathrm{T}}, \end{cases} \tag{20}$$

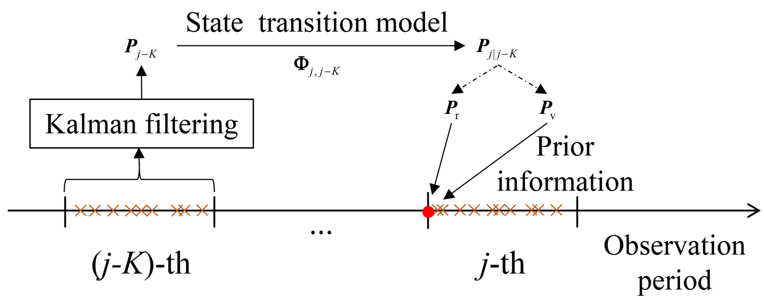

Figure 3 (Color online) Illustration of prior information generation and covariance propagation between observation periods. The covariance $\boldsymbol{P}_{j-K}$ from the $(j-K)$-th period is propagated through $\boldsymbol{\Phi}_{j,j-K}$ to form the prior covariance $\boldsymbol{P}_{j|j-K}$ for the j-th period, which provides the statistical basis for phase and Doppler frequency estimation.

where m_{ϕ_0} and $\sigma^2_{\phi_0}$ represent the mean and variance of ϕ_0^j, respectively. $\boldsymbol{P}_\mathrm{r} = \mathrm{Var}(\Delta \boldsymbol{r}_0^j)$ is the variance of the position estimation error, which corresponds to the position elements of the predicted covariance $\boldsymbol{P}_{j|j-K}$. The mean and variance of f_d are given by

$$\begin{cases} m_{f_\mathrm{d}} = 0, \\ \sigma^2_{f_\mathrm{d}} = f_\mathrm{s}^2 \left(\boldsymbol{G}_i \boldsymbol{\varphi}_1 \boldsymbol{P}_\mathrm{r} \boldsymbol{\varphi}_1^\mathrm{T} \boldsymbol{G}_i^\mathrm{T} + \boldsymbol{G}_i \boldsymbol{\gamma}_1 \boldsymbol{P}_\mathrm{v} \boldsymbol{\gamma}_1^\mathrm{T} \boldsymbol{G}_i^\mathrm{T} \right), \end{cases} \tag{21}$$

where m_{f_d} and $\sigma^2_{f_\mathrm{d}}$ represent the mean and variance of f_d, respectively. $\boldsymbol{P}_\mathrm{v} = \mathrm{Var}(\Delta \boldsymbol{v}_0^j)$ is the variance of the velocity estimation error, which corresponds to the velocity elements of the predicted covariance $\boldsymbol{P}_{j|j-K}$. The value of f_s can be expressed as

$$f_\mathrm{s} = f_0 + f_1 \cdot \left[g(\hat{t}^j_{i,\mathrm{sc}}) - T_0 \right]. \tag{22}$$

The joint probability density of the vector $\boldsymbol{\theta} = \left[\phi_0^j, f_\mathrm{d} \right]^\mathrm{T}$ is given by

$$p(\boldsymbol{\theta}) = \frac{1}{2\pi \left|\boldsymbol{\Sigma}\right|^{1/2}} \exp \left(-\frac{1}{2} \left(\boldsymbol{\theta} - \boldsymbol{m}\right)^\mathrm{T} \boldsymbol{\Sigma}^{-1} \left(\boldsymbol{\theta} - \boldsymbol{m}\right) \right), \tag{23}$$

where $\boldsymbol{m} = [m_{\phi_0}, m_{f_\mathrm{d}}]^\mathrm{T}$ is the mean vector, $|\boldsymbol{\Sigma}|$ is the determinant of the covariance matrix. The covariance matrix $\boldsymbol{\Sigma}$ is given by

$$\boldsymbol{\Sigma} = \begin{bmatrix} \sigma^2_{\phi_0} & \rho \sigma_{\phi_0} \sigma_{f_\mathrm{d}} \\ \rho \sigma_{\phi_0} \sigma_{f_\mathrm{d}} & \sigma^2_{f_\mathrm{d}} \end{bmatrix}, \tag{24}$$

where ρ is the correlation coefficient between ϕ_0^j and f_d, and it is expressed as

$$\rho = \frac{\mathrm{Cov}\left(\phi_0^j, f_\mathrm{d}\right)}{\sqrt{\mathrm{Var}\left(\phi_0^j\right) \mathrm{Var}\left(f_\mathrm{d}\right)}} = \frac{f_0^2 \boldsymbol{G}_0 \boldsymbol{P}_r \boldsymbol{G}_i^\mathrm{T} \boldsymbol{\varphi}_1^\mathrm{T}}{\sigma_{\phi_0} \sigma_{f_\mathrm{d}}}. \tag{25}$$

This prior modeling approach is valid when spacecraft dynamics remain smooth and the SNR is sufficiently high, ensuring that linearization and Gaussian assumptions hold. If the spacecraft experiences strong maneuvers, low SNR, or an excessively large K, the accuracy of the propagated covariance may degrade. In such cases, reducing K or reinitializing the Kalman filter is recommended.

3 Estimation model and algorithm

3.1 Estimation model

3.1.1 *Bayesian model based on prior information*

The objective function established by MLE does not utilize prior information of the unknown parameters, making it difficult to balance both estimation accuracy and real-time performance. The analysis in Section 2 shows that the unknown parameters follow a Gaussian distribution, and thus, within the Bayesian estimation framework, the prior information of the parameters can be used to construct the objective function.

The joint probability density of photon arrival times is given by

$$p\left(\{t_i^j\}_{i=0}^N|\boldsymbol{\theta}\right)=\exp\left[-\int_{t_0^j}^{t_N^j}\lambda(\tau_i)\mathrm{d}\tau\right]\prod_{i=0}^N\lambda(\tau_i), \tag{26}$$

where $\boldsymbol{\theta}=[\phi_0^j,f_\mathrm{d}]^\mathrm{T}$ represents the parameter to be estimated. The prior distribution of $\boldsymbol{\theta}$ is as shown in (23). Therefore, according to Bayes' theorem, the posterior probability distribution of the parameter $\boldsymbol{\theta}$ is

$$p\left(\boldsymbol{\theta}|\{t_i^j\}_{i=0}^N\right)=\frac{p\left(\{t_i^j\}_{i=0}^N|\boldsymbol{\theta}\right)\cdot p\left(\boldsymbol{\theta}\right)}{p\left(\{t_i^j\}_{i=0}^N\right)}. \tag{27}$$

Introducing a loss function $\ell(\boldsymbol{\vartheta},\boldsymbol{\theta})$, the Bayesian risk function is

$$R(\boldsymbol{\vartheta}|\{t_i^j\}_{i=0}^N)=\int_{\boldsymbol{\Theta}}\ell(\boldsymbol{\vartheta},\boldsymbol{\theta})p\left(\boldsymbol{\theta}|\{t_i^j\}_{i=0}^N\right)\mathrm{d}\boldsymbol{\theta}, \tag{28}$$

where $\boldsymbol{\Theta}=\{\boldsymbol{\theta}\}$ represents the parameter space, and $\boldsymbol{\vartheta}$ can be regarded as an estimate of $\boldsymbol{\theta}$. The loss function $\ell(\boldsymbol{\vartheta},\boldsymbol{\theta})$ measures the loss incurred when making a decision $\boldsymbol{\vartheta}$, while the true parameter is $\boldsymbol{\theta}$. The Bayesian risk function $R(\cdot)$ quantifies the expected loss associated with choosing $\boldsymbol{\vartheta}$ as an estimate of $\boldsymbol{\theta}$ given the data $\{t_i^j\}_{i=0}^N$.

Therefore, the optimal decision that minimizes the Bayesian risk corresponds to the Bayesian estimator, i.e.,

$$\boldsymbol{\vartheta}^*=\arg\min_{\boldsymbol{\vartheta}}R(\boldsymbol{\vartheta}|\{t_i^j\}_{i=0}^N). \tag{29}$$

There exist various choices for the loss function, such as the 0-1 loss function, squared error loss function, and linear loss function. Additionally, custom loss functions can be defined based on specific requirements. By selecting different loss functions, Eq. (29) takes different forms, highlighting the flexibility and generality of using the Bayesian risk function for phase and Doppler frequency estimation.

In this study, the 0-1 loss function is adopted, which penalizes any estimation error equally. Under the 0-1 loss, minimizing the Bayesian risk is equivalent to maximizing the posterior probability density function. Consequently, the optimal estimator reduces to the maximum a posteriori (MAP) estimator, given by

$$\hat{\boldsymbol{\theta}}=\arg\max_{\boldsymbol{\theta}}p\left(\boldsymbol{\theta}|\{t_i^j\}_{i=0}^N\right), \tag{30}$$

where $\hat{\boldsymbol{\theta}}$ is the optimal estimate of the unknown parameter $\boldsymbol{\theta}$, which is equivalent to $\boldsymbol{\vartheta}^*$ in (29).

3.1.2 *Objective function with interval-bounded constraints*

For computational convenience, the Bayesian estimation problem can be equivalently reformulated as the minimization of the negative log-posterior density. Accordingly, the objective function is defined as

$$J(\boldsymbol{\theta})\triangleq-\ln p(\boldsymbol{\theta}|\{t_i^j\}_{i=0}^N)=-\ln p(\{t_i^j\}_{i=0}^N|\boldsymbol{\theta})-\ln p(\boldsymbol{\theta}). \tag{31}$$

In (31), $\ln p(\{t_i^j\}_{i=0}^N|\boldsymbol{\theta})$ corresponds to the objective function of MLE, indicating that the Bayesian estimation model incorporates both MLE and prior parameter information. Thus, obtaining the optimal estimates of ϕ_0^j and f_d can be equivalent to minimizing the Bayesian estimation model:

$$\left(\hat{\phi}_0^j,\hat{f}_\mathrm{d}\right)=\mathop{\arg\min}_{\phi_0^j\in[0,1),f_\mathrm{d}\in F_D}J\left(\phi_0^j,f_\mathrm{d}\right), \tag{32}$$

where F_D represents the possible range of frequency values.

The parameter search space in the objective function defined by (32) is excessively broad, which poses challenges for both grid search methods and iterative optimization techniques. For grid search methods, a finer search step improves estimation accuracy but significantly reduces computational speed. When the parameter search range is too large, it becomes difficult to balance estimation accuracy and computational efficiency. For iterative optimization algorithms, the convexity of the objective function and the choice of initial values greatly influence the optimization results. A large parameter search range increases the likelihood that the objective function is non-convex, and the chosen initial values may be far from the true values, making the algorithm more susceptible to local optima. Therefore, imposing interval-bounded constraints based on prior information is essential.

Section 2 has demonstrated that, under prior information, the parameters to be estimated follow a normal distribution:

$$\begin{cases} \phi_0^j \sim \mathcal{N}(\widetilde{\phi}_0^j, \sigma_{\phi_0}^2), \\ f_{\mathrm{d}} \sim \mathcal{N}(0, \sigma_{f_{\mathrm{d}}}^2). \end{cases} \tag{33}$$

According to the properties of the normal distribution, the probabilities that ϕ_0 and f_{d} lie within the intervals $[\widetilde{\phi}_0^j - 3\sigma_{\phi_0}, \widetilde{\phi}_0^j + 3\sigma_{\phi_0}]$ and $[-3\sigma_{f_{\mathrm{d}}}, 3\sigma_{f_{\mathrm{d}}}]$, respectively, are as high as 99.74%. Therefore, we define the search space $\Omega = [\widetilde{\phi}_0^j - 3\sigma_{\phi_0}, \widetilde{\phi}_0^j + 3\sigma_{\phi_0}] \times [-3\sigma_{f_{\mathrm{d}}}, 3\sigma_{f_{\mathrm{d}}}]$, which allows us to reasonably assume that the true values of ϕ_0^j and f_{d} lie within this region. Consequently, the objective function defined in (32) is equivalent to the interval-bounded constrained objective function:

$$\hat{\boldsymbol{\theta}} = \arg\min J(\boldsymbol{\theta}), \qquad \text{s.t. } \boldsymbol{\theta} \in \Omega. \tag{34}$$

To investigate the convexity of the objective function within the search space, an analysis of its second-order local geometric properties is required. In the following analysis, $J(\boldsymbol{\theta})$ denotes the negative log-posterior objective function. The Hessian matrix of $J(\boldsymbol{\theta})$ is given by

$$\boldsymbol{B}_J = \nabla^2 J(\boldsymbol{\theta}) = \boldsymbol{\Sigma}^{-1} - \boldsymbol{B}_L(\boldsymbol{\theta}), \tag{35}$$

where $\boldsymbol{B}_L(\boldsymbol{\theta}) = \nabla^2 \ln p(\{t_i^j\}_{i=0}^N|\boldsymbol{\theta})$ denotes the Hessian matrix of the log-likelihood term. Since the prior distribution is Gaussian, the Hessian of the negative log-prior term is given by the constant positive definite matrix $\boldsymbol{\Sigma}^{-1}$.

Convexity of the objective function over the search space Ω requires

$$\boldsymbol{B}_J(\boldsymbol{\theta}) \succ 0, \qquad \forall \boldsymbol{\theta} \in \Omega. \tag{36}$$

By applying Weyl's eigenvalue inequality, the minimum eigenvalue of $\boldsymbol{B}_J(\boldsymbol{\theta})$ satisfies

$$l_{\min}[\boldsymbol{B}_J(\boldsymbol{\theta})] \geqslant \frac{1}{l_{\max}(\boldsymbol{\Sigma})} - l_{\max}[\boldsymbol{B}_L(\boldsymbol{\theta})], \tag{37}$$

where $l_{\min}(\cdot)$ and $l_{\max}(\cdot)$ denote the minimum and maximum eigenvalues of the matrix, respectively. Accordingly, a sufficient condition for the convexity of the objective function over the search space is given by

$$l_{\max}[\boldsymbol{B}_L(\boldsymbol{\theta})] < \frac{1}{l_{\max}(\boldsymbol{\Sigma})}, \qquad \forall \boldsymbol{\theta} \in \Omega. \tag{38}$$

According to (24), the maximum eigenvalue of $\boldsymbol{\Sigma}$ admits the closed-form expression

$$l_{\max}(\boldsymbol{\Sigma}) = \frac{1}{2}\left[\sigma_{\phi_0}^2 + \sigma_{f_d}^2 + \sqrt{\left(\sigma_{\phi_0}^2 - \sigma_{f_d}^2\right)^2 + 4\rho^2\sigma_{\phi_0}^2\sigma_{f_d}^2}\right]. \tag{39}$$

To facilitate quantitative analysis, a dimensionless parameter is introduced as

$$\mathcal{L} = \sup_{\boldsymbol{\theta}\in\Omega} \{l_{\max}[\boldsymbol{B}_L(\boldsymbol{\theta})] \cdot l_{\max}(\boldsymbol{\Sigma})\} \tag{40}$$

based on which a compact sufficient condition for convexity can be expressed as

$$\mathcal{L} < 1, \qquad \forall \boldsymbol{\theta} \in \Omega. \tag{41}$$

The above analysis shows that the non-convexity of the original objective function originates solely from the log-likelihood term. By introducing Gaussian prior information, a constant positive definite curvature term is added to the Hessian of the negative log-posterior. When the parameter space is restricted to a high-probability interval induced by the prior, the curvature of the log-likelihood term becomes uniformly bounded. Consequently, if the maximum curvature of the log-likelihood term within the constrained search space is sufficiently dominated by the inverse prior covariance, the resulting objective function can be shown to be strictly convex over the constrained search space. This provides a theoretical justification for treating the interval-bounded objective function as convex in the design of the F-BFGS-B optimization algorithm.

3.2 Fast non-convex optimization estimation method

3.2.1 *F-BFGS-B algorithm*

Through (34), a convex objective function under interval boundary constraints is obtained. In theory, convex optimization methods can be employed to solve it. However, the interval boundary constraints are based on the prior variance, which does not always guarantee that a non-convex function is transformed into a convex function. For instance, when the prior variance is significantly large, the corresponding parameter interval also becomes extensive, making it difficult to ensure that the objective function remains entirely convex over the large interval. Therefore, to enhance the adaptability of the proposed method under various conditions, this subsection introduces F-BFGS-B, an improved algorithm based on BFGS.

BFGS is a quasi-Newton optimization method that does not require the computation of the second-order Hessian matrix while achieving a fast convergence rate. It is one of the most widely used quasi-Newton methods. Let $\boldsymbol{B}_k$ be the approximation Hessian matrix at the k-th iteration, and then the rank-two update formula for $\boldsymbol{B}_k$ is given by

$$\boldsymbol{B}_k = \boldsymbol{B}_{k-1} + \beta \boldsymbol{u}\boldsymbol{u}^{\mathrm{T}} + \gamma \boldsymbol{v}\boldsymbol{v}^{\mathrm{T}}. \tag{42}$$

where $\beta, \gamma \in \mathbb{R}$ and $\boldsymbol{u}, \boldsymbol{v} \in \mathbb{R}^n$. Substituting the rank-two update of $\boldsymbol{B}_k$ into the quasi-Newton equation yields the BFGS approximation matrix

$$\boldsymbol{B}_k = \boldsymbol{B}_{k-1} + \frac{\boldsymbol{y}_{k-1}\boldsymbol{y}_{k-1}^{\mathrm{T}}}{\boldsymbol{y}_{k-1}^{\mathrm{T}}\boldsymbol{s}_{k-1}} - \frac{\boldsymbol{B}_{k-1}\boldsymbol{s}_{k-1}\boldsymbol{s}_{k-1}^{\mathrm{T}}\boldsymbol{B}_{k-1}}{\boldsymbol{s}_{k-1}^{\mathrm{T}}\boldsymbol{B}_{k-1}\boldsymbol{s}_{k-1}}, \tag{43}$$

where $\boldsymbol{s}_k = \boldsymbol{\theta}_k - \boldsymbol{\theta}_{k-1}$ and $\boldsymbol{y}_k = \nabla \boldsymbol{J}(\boldsymbol{\theta}_{k+1}) - \nabla \boldsymbol{J}(\boldsymbol{\theta}_k)$. If $\boldsymbol{H}_k$ is the inverse of the approximated Hessian matrix, then using the Sherman-Morrison-Woodbury formula, the inverse matrix can be expressed as

$$\boldsymbol{H}_k = \boldsymbol{H}_{k-1} + \left(1 + \frac{\boldsymbol{y}_{k-1}^{\mathrm{T}}\boldsymbol{H}_{k-1}\boldsymbol{y}_{k-1}}{\boldsymbol{y}_{k-1}^{\mathrm{T}}\boldsymbol{s}_{k-1}}\right)\frac{\boldsymbol{s}_{k-1}^{\mathrm{T}}\boldsymbol{s}_{k-1}}{\boldsymbol{y}_{k-1}^{\mathrm{T}}\boldsymbol{s}_{k-1}} - \frac{\boldsymbol{s}_{k-1}\boldsymbol{y}_{k-1}^{\mathrm{T}}\boldsymbol{H}_{k-1}}{\boldsymbol{y}_{k-1}^{\mathrm{T}}\boldsymbol{s}_{k-1}} - \frac{\boldsymbol{H}_{k-1}\boldsymbol{y}_{k-1}\boldsymbol{s}_{k-1}^{\mathrm{T}}}{\boldsymbol{y}_{k-1}^{\mathrm{T}}\boldsymbol{s}_{k-1}}. \tag{44}$$

Eq. (44) is the core formula of the BFGS algorithm. After calculating $\boldsymbol{H}_k$, the search direction $\boldsymbol{p}_k = -\boldsymbol{H}_k \cdot \nabla \boldsymbol{J}(\boldsymbol{\theta}_k)$ can be obtained, and then the step size can be calculated using linear search. Finally, the unknown parameters are iteratively updated.

However, in the problem of phase and Doppler frequency estimation, the BFGS method has two issues. The first issue is to use a linear search method to determine the step size α. Traditional line search criteria mainly include the Armijo condition and the Wolfe condition. However, line search methods are slow and search for a one-dimensional numerical step size, which does not meet the requirements for the rapid optimization of the objective function.

To address the first issue, this subsection introduces an adaptive step size adjustment method based on first-order and second-order moment estimations of the search direction. This approach automatically adjusts the step size for each parameter. The first-order moment estimate $\boldsymbol{m}_k^p$ and second-order moment estimate $\boldsymbol{v}_k^p$ of the descent direction are updated as follows:

$$\begin{cases} \boldsymbol{m}_k^p = \beta_1 \boldsymbol{m}_{k-1}^p + (1-\beta_1)\boldsymbol{p}_k, \\ \boldsymbol{v}_k^p = \beta_2 \boldsymbol{v}_{k-1}^p + (1-\beta_2)\boldsymbol{p}_k^2, \end{cases} \tag{45}$$

where β_1 and β_2 are the exponential decay rates for the first-order and second-order moment estimates, typically set to values greater than 0.9. The moment estimates $\boldsymbol{m}_k^p$ and $\boldsymbol{v}_k^p$ accumulate historical search direction information. Next, the current search direction undergoes exponential decay to obtain the bias-corrected estimate $\hat{\boldsymbol{p}}$:

$$\hat{\boldsymbol{p}}_k = \frac{\boldsymbol{p}_k}{1-\beta_1^k}. \tag{46}$$

Then, Nesterov momentum (NM) is applied to accelerate convergence and perform bias correction, yielding the corrected first-order and second-order moment estimates:

$$\begin{cases} \hat{\boldsymbol{m}}_k^p = \dfrac{\boldsymbol{m}_k^p}{1-\beta_1^k}, \\ \hat{\boldsymbol{v}}_k^p = \dfrac{\boldsymbol{v}_k^p}{1-\beta_2^k}. \end{cases} \tag{47}$$

The adjusted step size is then computed as

$$\boldsymbol{\alpha}_k = \frac{\alpha_0}{\sqrt{\hat{\boldsymbol{v}}_k^p + \epsilon}}, \tag{48}$$

where α_0 is the initial step size, and ϵ is a small positive value to prevent division by zero. The updated search direction is given by

$$\overline{\boldsymbol{p}}_k = (1 - \beta_1) \cdot \hat{\boldsymbol{p}}_k + \beta_1 \cdot \hat{\boldsymbol{m}}_k^p. \tag{49}$$

Compared to line search methods that require iterative computation of step size, this approach leverages Nesterov momentum acceleration and exponential decay to directly determine the search step size. This significantly improves the overall convergence speed of the algorithm.

For the second issue, various methods exist for handling unknown parameter boundary constraints, such as the projection method, penalty function method, and Lagrangian method. The projection method is straightforward but may result in failed parameter updates. Meanwhile, the penalty function and Lagrangian methods are more complex. To address this problem efficiently, this paper defines a nonlinear transformation function that maps estimated values exceeding the constraint interval back into the valid range. This approach prevents parameter update failures while maintaining simplicity. The nonlinear mapping function is defined as

$$\boldsymbol{\theta}_k = \boldsymbol{\theta}_{\mathrm{l}} + \frac{\boldsymbol{\theta}_{\mathrm{u}} - \boldsymbol{\theta}_{\mathrm{l}}}{1 + \exp(-\boldsymbol{\theta}_k)}, \tag{50}$$

where $\boldsymbol{\theta}_{\mathrm{l}}$ and $\boldsymbol{\theta}_{\mathrm{u}}$ represent the lower and upper bounds of the constrained parameter space, respectively.

The stopping condition of an iterative optimization algorithm is a crucial factor. As mentioned in the first issue, when the gradient of the objective function is too large, it may not be feasible to use the gradient as a termination criterion. Therefore, this paper adopts the parameter change as the stopping condition, defined as

$$|\boldsymbol{\theta}_{k+1} - \boldsymbol{\theta}_k| < \varepsilon. \tag{51}$$

Based on BFGS and (45)–(51), the pseudo-code of the F-BFGS-B algorithm is shown in Algorithm 1. The proposed F-BFGS-B algorithm introduces adaptive step size adjustment using first- and second-order moment estimates of the search direction. Additionally, a nonlinear mapping function ensures that parameter updates remain within predefined constraints. By integrating these improvements, the algorithm enhances convergence speed and robustness in constrained optimization problems.

Algorithm 1 F-BFGS-B Algorithm.

Require: $\boldsymbol{\theta}_0$, ε, ϵ, α_0, $\boldsymbol{\theta}_{\mathrm{l}}$, $\boldsymbol{\theta}_{\mathrm{u}}$, $N_{\max}$.
Ensure: Optimal solution $\boldsymbol{\theta}^*$.
$k \leftarrow 0$;
$\boldsymbol{\theta} \leftarrow \boldsymbol{\theta}_0$;
$\boldsymbol{H}_0 \leftarrow \boldsymbol{I}$; {Initialize the approximate inverse Hessian matrix}
repeat
  $\boldsymbol{g}_k \leftarrow \nabla \boldsymbol{J}(\boldsymbol{\theta}_k)$; {Compute the gradient}
  $\boldsymbol{p}_k \leftarrow -\boldsymbol{H}_k \boldsymbol{g}_k$; {Compute the search direction}
  $\boldsymbol{m}_k^p \leftarrow \beta_1 \boldsymbol{m}_{k-1}^p + (1-\beta_1)\boldsymbol{p}_k$;
  $\boldsymbol{v}_k^p \leftarrow \beta_2 \boldsymbol{v}_{k-1}^p + (1-\beta_2)\boldsymbol{p}_k^2$;
  $\hat{\boldsymbol{p}}_k \leftarrow \frac{\boldsymbol{p}_k}{1-\beta_1^k}$;
  $\hat{\boldsymbol{m}}_k^p \leftarrow \frac{\boldsymbol{m}_k^p}{1-\beta_1^k}$;
  $\hat{\boldsymbol{v}}_k^p \leftarrow \frac{\boldsymbol{v}_k^p}{1-\beta_2^k}$;
  $\boldsymbol{\alpha}_k \leftarrow \frac{\alpha_0}{\sqrt{\hat{\boldsymbol{v}}_k^p + \epsilon}}$; {Adjust step size}
  $\overline{\boldsymbol{p}}_k \leftarrow (1-\beta_1) \cdot \hat{\boldsymbol{p}}_k + \beta_1 \cdot \hat{\boldsymbol{m}}_k^p$;
  $\boldsymbol{\theta}_{k+1} \leftarrow \boldsymbol{\theta}_k + \boldsymbol{\alpha}_k \overline{\boldsymbol{p}}_k$;
  $\boldsymbol{\theta}_{k+1} \leftarrow$ (50);
  $\boldsymbol{s}_{k+1} \leftarrow \boldsymbol{\theta}_{k+1} - \boldsymbol{\theta}_k$;
  if $\|\boldsymbol{s}_{k+1}\| < \varepsilon$ **then**
    break
  end if
  $\boldsymbol{y}_{k+1} \leftarrow \nabla \boldsymbol{J}(\boldsymbol{\theta}_{k+1}) - \nabla \boldsymbol{J}(\boldsymbol{\theta}_k)$;
  $\boldsymbol{H}_{k+1} \leftarrow$ (44);
  $k \leftarrow k+1$;
until $k \geqslant N_{\max}$ or $\|\boldsymbol{s}_{k+1}\| < \varepsilon$;
return $\boldsymbol{\theta}$.

3.2.2 *Convergence analysis and discussion of F-BFGS-B*

The F-BFGS-B algorithm is an improved method based on Nadam and BFGS. Its main idea is to use the second-order curvature information provided by BFGS to modify the first-order search direction of Nadam, thereby enhancing the convergence speed and stability of the algorithm while maintaining the adaptive characteristics. Therefore, in this subsection, we present a discussion and analysis of the convergence rationality of the algorithm based on existing theoretical frameworks.

The convergence of the Nadam algorithm has been systematically proven in several studies [32, 33]. Under the assumptions that the objective function is lower bounded, the gradient is Lipschitz continuous, and the second moment of the gradient is bounded, Nadam can converge to a stationary point. Within this framework, F-BFGS-B introduces the inverse Hessian matrix $\boldsymbol{H}_k$ from BFGS to incorporate local curvature information. The update rules of the algorithm are shown in (45)–(49) or in Algorithm 1. Since the BFGS update preserves the positive definiteness of the matrix, the search direction $-\boldsymbol{H}_k \cdot \nabla \boldsymbol{J}(\boldsymbol{\theta}_k)$ is always a descent direction, which ensures that the objective function decreases monotonically in the expectation sense. It can thus be seen that F-BFGS-B retains the convergence framework of Nadam, and the BFGS preconditioning only changes the scale of the search direction without destroying its convergence property.

In terms of the adaptive step-size mechanism, F-BFGS-B inherits the structure of Nadam. Its second-moment estimation $\boldsymbol{v}_k^p$ and bias-correction $\hat{\boldsymbol{v}}_k^p$ forms are given in (45) and (47), respectively, and the bias correction $\hat{\boldsymbol{v}}_k^p$ is an exponentially weighted average of past squared gradients. Because the weighting coefficients are decreasing and non-negative, the quantity is non-decreasing in expectation and eventually convergent. Therefore, the corresponding adjusted step size $\boldsymbol{\alpha}_k$ exhibits an overall decreasing trend and tends to stabilize in the later stages of iteration. Although in certain local iterations gradient fluctuations may cause a slight increase in step size, the overall trend still gradually decreases with the iteration process, ensuring numerical stability and smooth convergence of the algorithm. This adaptive adjustment mechanism enables F-BFGS-B to perform rapid exploration with a relatively large step size at the early stage of iteration and to automatically reduce the step size during the convergence phase, thereby suppressing oscillations. The second-order preconditioning of BFGS plays a key role in this process. Since $\boldsymbol{H}_k$ provides local curvature information, F-BFGS-B essentially realizes a coupled adjustment of adaptive step size and second-order scaling based on Nadam. From a theoretical perspective, this combination improves the scale consistency of parameter updates across different dimensions.

3.3 Posterior CRLB based on prior information

Ashby et al. [34] derived the CRLB for the joint estimation of phase and Doppler shift, and the expression is given as

$$\mathrm{CRLB}\left(\hat{\phi}_0^j, \hat{f}_\mathrm{d}\right) = \frac{1}{L}\begin{bmatrix} 4T_\mathrm{obs}^{-1} & -6T_\mathrm{obs}^{-2} \\ -6T_\mathrm{obs}^{-2} & 12T_\mathrm{obs}^{-3} \end{bmatrix}, \tag{52}$$

where L is determined by the standard pulse profile and the flux parameters of the pulsar, and it can be calculated according to (B11). The CRLB corresponding to (52) for the joint estimation of position and velocity can be expressed as [34]

$$\mathrm{CRLB}\left(\hat{x}, \hat{v}\right) = \frac{c^2}{f_0^2 L}\begin{bmatrix} 4T_\mathrm{obs}^{-1} & -6T_\mathrm{obs}^{-2} \\ -6T_\mathrm{obs}^{-2} & 12T_\mathrm{obs}^{-3} \end{bmatrix}, \tag{53}$$

where $\hat{x}$ and $\hat{v}$ denote the estimated position and velocity, respectively.

Compared to traditional estimation methods, the phase and Doppler frequency model incorporating prior information can be viewed as estimating these parameters under known prior conditions. Consequently, the posterior CRLB (PCRLB) can be derived analogously to the CRLB. From the derivations in Appendix B, the PCRLB for phase and Doppler frequency are given as

$$\mathrm{PCRLB}\left(\hat{\phi}_0^j, \hat{f}_\mathrm{d}\right) = \frac{1}{\Delta}\begin{bmatrix} I_{22} & -I_{12} \\ -I_{21} & I_{11} \end{bmatrix}, \tag{54}$$

Table 1 Parameters of Crab pulsar [12, 35].

Parameter	Value
Right ascension (°)	83.63
Declination (°)	22.01
D (kpc)	2
F_X (ph/cm^2/s)	1.54
W (10^{-3}s)	1.67
P (10^{-3}s)	33.4
P_f (%)	70
Right ascension error (mas)	5
Declination error (mas)	60

Table 2 Orbit parameters of Tianwen-1 [3].

Parameter	Value
Semi-major axis (km)	1.9770×10^8
Eccentricity	0.2326
Inclination (°)	23.5374
Right ascension of the ascending node (°)	358.844
Argument of periapsis (°)	298.716
True anomaly (°)	136.937

where $\Delta = I_{11}I_{22} - I_{12}^2$ can be calculated according to (B15). I_{11}, I_{12}, I_{21} and I_{22} can be expressed as

$$\begin{cases} I_{11} = LT_{\mathrm{obs}} + \dfrac{1}{(1-\rho^2)\sigma_{\phi_0}^2}, \\ I_{22} = \dfrac{LT_{\mathrm{obs}}^3}{3} + \dfrac{1}{(1-\rho^2)\sigma_{f_\mathrm{d}}^2}, \\ I_{12} = I_{21} = \dfrac{LT_{\mathrm{obs}}^2}{2} - \dfrac{\rho}{(1-\rho^2)\sigma_{\phi_0}\sigma_{f_\mathrm{d}}}. \end{cases} \tag{55}$$

Then, the PCRLB corresponding to (54) for the joint estimation of position and velocity can be expressed as

$$\mathrm{PCRLB}\,(\hat{x}, \hat{v}) = \frac{c^2}{f_0^2\Delta}\begin{bmatrix} I_{22} & -I_{12} \\ -I_{21} & I_{11} \end{bmatrix}. \tag{56}$$

4 Results and analysis

4.1 Simulation conditions

In this study, the Crab pulsar [12, 35] is selected as the observed pulsar. The reference time T_0 is set to January 15, 2021 (MJD = 59229), and its parameters are listed in Table 1. The detector area A_d is set to 30 cm^2 [36], with an observation period T_{obs} of 1800 s. The orbital parameters of the Tianwen-1 Mars probe [3] are listed in Table 2, with the simulation start time set to February 6, 2021, and the position and velocity error covariances set to $(20\ \mathrm{km})^2$ and $(20\ \mathrm{m/s})^2$, respectively. The FHPDE algorithm terminates early when the changes in phase and Doppler frequency are less than 1×10^{-6} and 1×10^{-9} Hz, respectively. Other parameters of FHPDE are listed in Table 3.

The simulation experiments were conducted on an Ubuntu 22.04 LTS system with a Linux kernel version 5.15.0-89-generic. The hardware setup consists of a 10 vCPU Intel Xeon processor (Skylake, IBRS) and an A100-PCIE-40GB GPU. The simulations were implemented using Python 3.9. All simulation results were obtained from 100 Monte Carlo trials. The performance of different methods was evaluated using the root mean square error (RMSE) and GPU execution time.

Table 3 Parameters of FHPDE.

Parameter	Value
Phase search range	$[\widetilde{\phi}_0 - 3\sigma_{\phi_0}, \widetilde{\phi}_0 + 3\sigma_{\phi_0}]$
Doppler frequency search range	$[-3\sigma_{f_0}, +3\sigma_{f_0}]$
Maximum iterations	10
α_0	1×10^{-8}
ϵ	1×10^{-8}
β_1	0.9
β_2	0.99

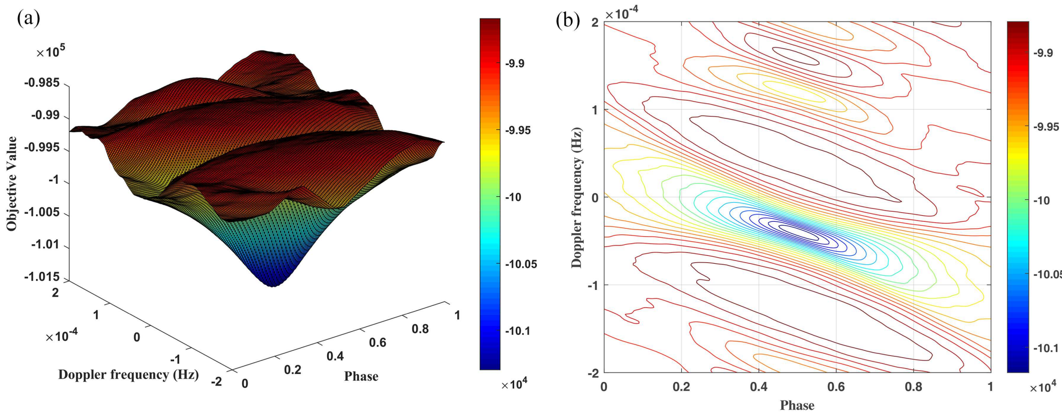

Figure 4 (Color online) Objective function values without prior information. (a) Three-dimensional distribution of the objective function values without prior information; (b) contour plot of the objective function without prior information.

4.2 Convergence results of the FHPDE

Before proceeding with the subsequent result analysis, this subsection first analyzes the convergence of the FHPDE method. The feasibility of the FHPDE method is demonstrated from two perspectives: the convexity of the objective function and the convergence process.

4.2.1 *Convexity analysis of the objective function*

This subsection explains and analyzes the convexity of the objective function, providing feasibility for the subsequent analysis. The simulation conditions remain consistent with Subsection 4.1, and the constraint interval based on prior information is determined according to (34).

Figure 4 illustrates the objective function value distribution without prior information. From Figure 4, it is visually evident that the traditional objective function without prior information is a non-convex function with multiple local minima. Figure 5 shows the distribution of the objective function values with prior information. The interval constraints determined by the prior information are set according to (34). From Figure 5, it can be observed that under the conditions of prior information and interval constraints, the objective function changes from a non-convex function to a convex function, allowing the optimization algorithm to estimate the optimal hyper-parameters.

Furthermore, by comparing Figures 4 and 5, it can be seen that the variation of the objective function in the phase direction is relatively smooth and uniform, with small gradient changes, while in the Doppler frequency direction, the changes are more abrupt, with larger gradient variations. This indicates that the objective function is more sensitive to changes in the Doppler frequency direction. Therefore, during the search for the optimal value, different search step sizes need to be set for the optimization algorithm in the phase and Doppler frequency directions. It is evident that the traditional BFGS algorithm, where all parameters to be estimated share the same search step size, is not applicable.

4.2.2 *Convergence analysis of the proposed method*

To assess the convergence performance of the proposed method, Figure 6 presents the optimization trajectories from six independent trials. In Figure 6, the red circles in each subplot mark the results of each iteration, while the red

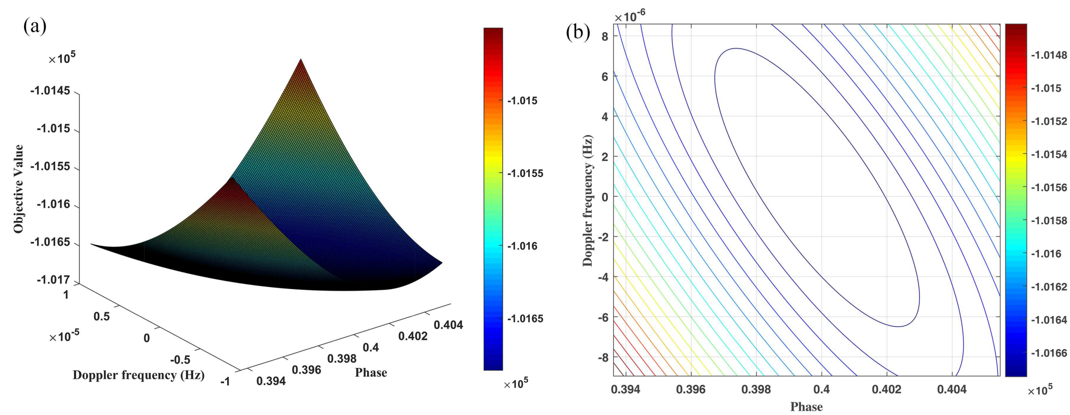

Figure 5 (Color online) Distribution of the objective function values with prior information. (a) Three-dimensional distribution of the objective function values with prior information; (b) contour plot of the objective function values with prior information.

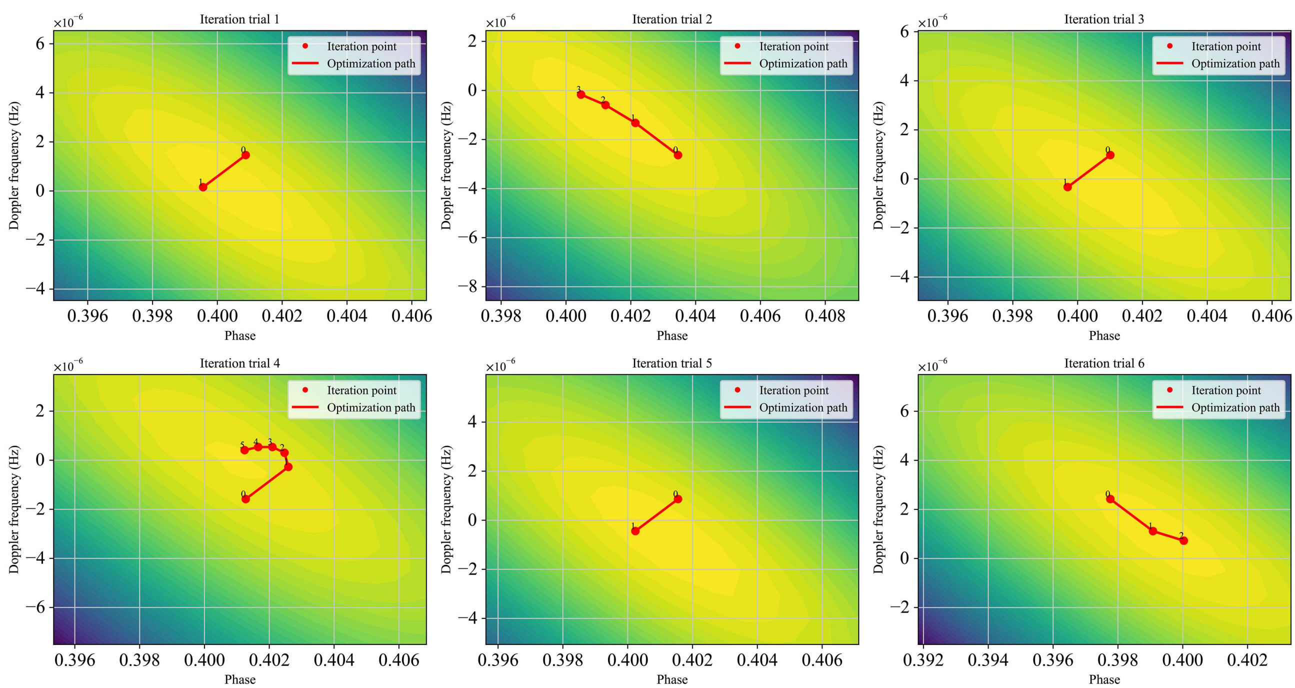

Figure 6 (Color online) Optimization trajectories of six different trials in the phase-Doppler frequency domain. The red circles represent the phase and Doppler frequency coordinates obtained after each iteration, while the red curves illustrate the optimization path, showing the trajectory of the algorithm as it gradually converges from the initial estimate to the final value. The numbers in each subplot indicate the sequence of iterations.

lines represent the optimization path, with numbered labels indicating the sequence of iterations (e.g., "0" represents the initial iteration). Each trajectory in the figure demonstrates that, within a limited number of iterations, the algorithm successfully converges to the desired results across different trials. The ground-truth values are set to 0.4 for phase and 0 Hz for Doppler frequency. Here, the true value of the Doppler frequency is 0 Hz because the enhanced on-orbit phase model presented in Section 2 compensates for the effect of the actual Doppler frequency.

As observed, the red paths in all subplots converge toward the vicinity of the ground-truth point, demonstrating the stability and robustness of the proposed algorithm under different initial conditions. Despite the varying starting points, each trajectory rapidly approaches the optimal solution within a limited number of iterations. Specifically, convergence is typically achieved within five steps, highlighting the high efficiency of the proposed method.

Moreover, the final estimates in all trials exhibit very low errors compared to the ground truth, confirming the algorithm's ability to achieve high-accuracy estimations. This further validates the effectiveness of the proposed approach in precisely estimating both phase and Doppler frequency.

Table 4 Parameters of GS-MLE and AGS.

Parameter	GS-MLE	AGS
Phase search range	[0, 1]	$[\widetilde{\phi}_0 - 3\sigma_{\phi_0}, \widetilde{\phi}_0 + 3\sigma_{\phi_0}]$
Doppler frequency search range	$[-2 \times 10^{-4},\ 2 \times 10^{4}]$	$[-3\sigma_{f_\mathrm{d}}, +3\sigma_{f_\mathrm{d}}]$
Interval size for phase search	0.0005	0.0005
Interval size for Doppler frequency search	1×10^{-6}	1×10^{-6}

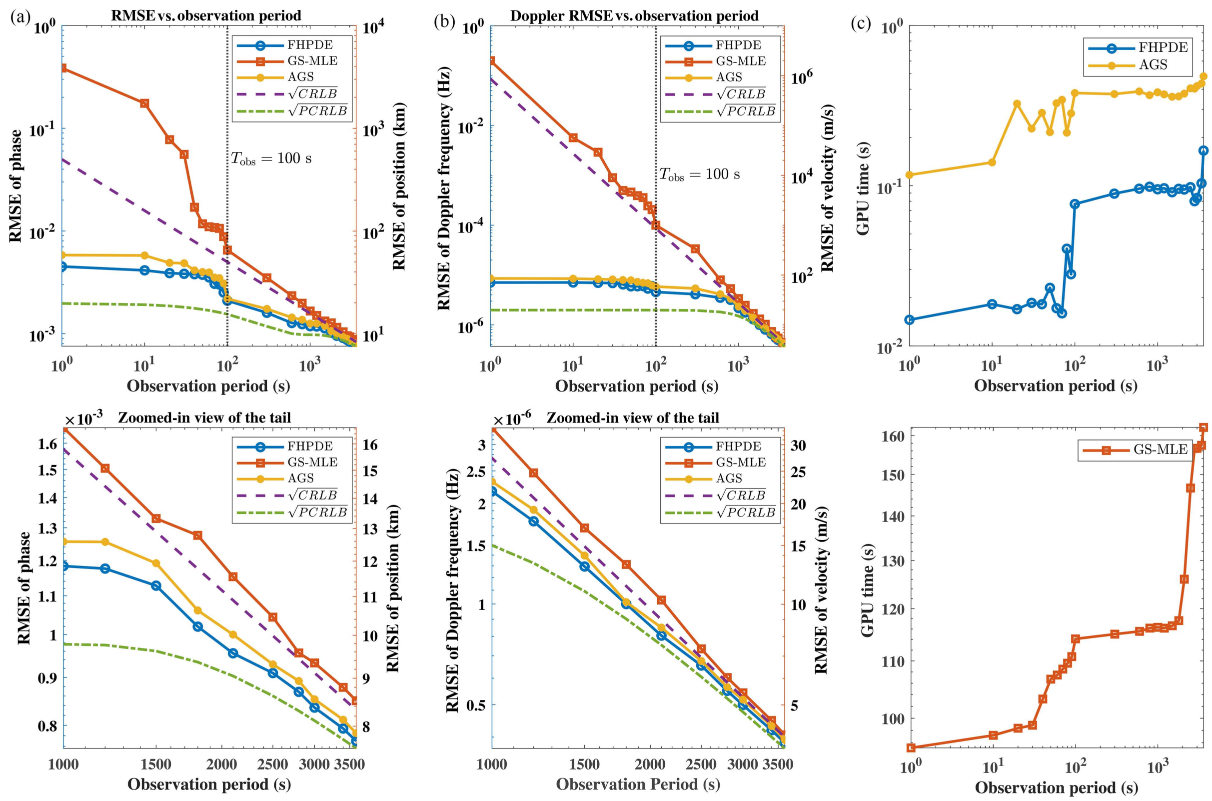

Figure 7 (Color online) Performance comparison of the three estimation methods under different observation periods. (a) Comparison of phase estimation errors; (b) comparison of Doppler frequency shift estimation errors; (c) comparison of GPU computation time. FHPDE: the proposed method. GS-MLE: the grid search method based on MLE. AGS: the adaptive grid search method [25].

4.3 Performance comparison under different observation periods

In this subsection, the FHPDE algorithm is compared with the grid search method based on MLE (GS-MLE) and the AGS method [25] using simulation data. The prior information for AGS is also determined according to (34). The simulation conditions remain consistent with Subsection 4.1. The parameters of the two methods, GS-MLE and AGS, are presented in Table 4. Figure 7 illustrates the variation in the performance of the three different estimation methods as a function of the observation period. In both Figures 7(a) and (b), the bottom subplots provide a magnified view of the tail section of the top curves.

From the simulation results, it can be observed that when the observation time is short (less than 100 s), the FHPDE and AGS algorithms maintain stable estimation accuracy, whereas the performance of GS-MLE deteriorates significantly. This degradation occurs because GS-MLE lacks effective prior constraints under limited photon counts, resulting in large fluctuations in the estimation results. In contrast, FHPDE and AGS utilize prior information to restrict the parameter search range, effectively limiting the upper bound of the estimation error. When the observation period ranges from 100 to 1000 s, the estimation errors of FHPDE and AGS are notably lower than those of GS-MLE. As the observation period increases beyond 2000 s, the performance differences among the three methods gradually diminish and eventually converge to the theoretical lower bounds (CRLB or PCRLB). This indicates that, with longer observation durations, the detector accumulates more photons and obtains richer information, thereby reducing the impact of prior constraints on estimation performance.

In terms of computational efficiency, FHPDE exhibits a remarkable advantage in real-time performance. Experimental results show that for short observation periods (1–100 s), the average GPU computation time of FHPDE

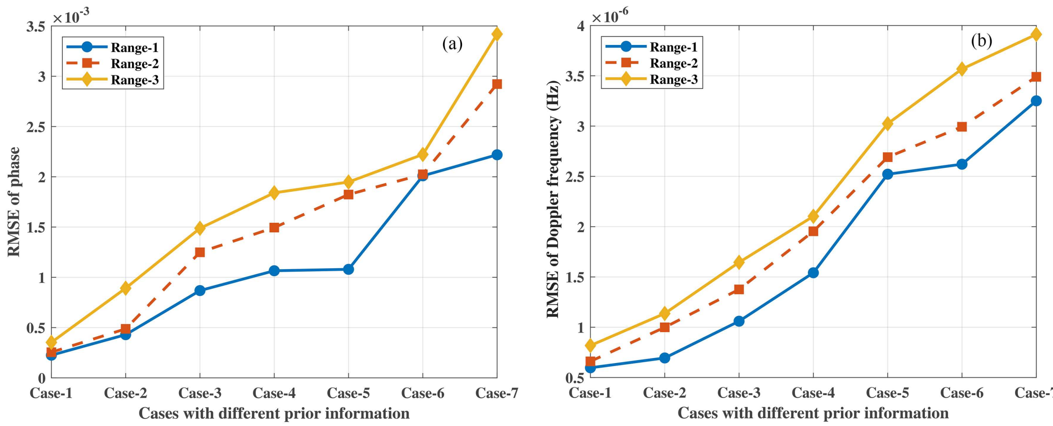

Figure 8 (Color online) Estimation under different search ranges and prior information. (a) Phase estimation error; (b) Doppler frequency error. Range-1: $[\boldsymbol{m}-\boldsymbol{\sigma_\theta}, \boldsymbol{m}+\boldsymbol{\sigma_\theta}]$. Range-2: $[\boldsymbol{m}-2\boldsymbol{\sigma_\theta}, \boldsymbol{m}+2\boldsymbol{\sigma_\theta}]$. Range-3: $[\boldsymbol{m}-3\boldsymbol{\sigma_\theta}, \boldsymbol{m}+3\boldsymbol{\sigma_\theta}]$. The settings of different prior information are listed in Table 5.

is less than 0.05 s. In contrast, GS-MLE requires considerably longer computation time even for short observation windows, limiting its applicability to real-time scenarios. The computation time of AGS is slightly higher than that of FHPDE but remains much lower than GS-MLE, primarily due to its adaptive search mechanism. Overall, FHPDE achieves the highest computational efficiency, as it eliminates the need for grid search, converges rapidly, and requires fewer objective function evaluations. For instance, when the observation period is 1800 s, the GPU computation times of FHPDE, GS-MLE, and AGS are 0.095, 117.626, and 0.361 s, respectively. Compared with GS-MLE and AGS, the computation time of FHPDE is reduced by 99.91% and 73.68%, respectively. Furthermore, as illustrated in Figure 7, the GPU computation times of AGS and FHPDE do not always increase monotonically with the observation duration. This is because their computation time depends not only on the observation length but also on the prior information and the size of the search interval. Although minor fluctuations exist, the overall trend remains increasing.

In summary, the FHPDE algorithm demonstrates excellent stability and real-time performance under both short and long observation periods. In the short-term observation stage, prior information plays a dominant role, effectively constraining the upper bound of estimation errors. In the long-term observation stage, photon observation data gradually become the dominant information source, allowing the estimation results to approach the theoretical limit (PCRLB). These findings confirm that the proposed algorithm achieves high accuracy and efficiency across various observation time domains.

4.4 Robustness analysis with respect to prior information and search range variability

This subsection aims to evaluate the robustness of the proposed FHPDE method with respect to the accuracy of prior information and the variability of the search range. Specifically, we assess the algorithm's sensitivity to different levels of prior state covariance and parameter search intervals. The different prior information refers mainly to the covariance of spacecraft state errors, with each case corresponding to the covariance values listed in Table 5. In Table 5, $\mathcal{D}(\cdot)$ denotes the main diagonal elements of the matrix, covering prior information with varying levels of accuracy. The search ranges are set as follows: $[\boldsymbol{m}-\boldsymbol{\sigma_\theta}, \boldsymbol{m}+\boldsymbol{\sigma_\theta}]$, $[\boldsymbol{m}-2\boldsymbol{\sigma_\theta}, \boldsymbol{m}+2\boldsymbol{\sigma_\theta}]$, and $[\boldsymbol{m}-3\boldsymbol{\sigma_\theta}, \boldsymbol{m}+3\boldsymbol{\sigma_\theta}]$, which are referred to as Range-1, Range-2, and Range-3, respectively. Figure 8 presents the phase and Doppler frequency shift estimation errors under different search ranges and prior information conditions.

Figure 8 illustrates the estimation errors of phase and Doppler frequency shift under different search ranges and prior information conditions. As shown in Figure 8, it can be observed that when the search range remains constant, the estimation error increases as the prior covariance increases. Similarly, when the prior covariance remains unchanged, the estimation error increases as the search range expands. An increase in the search range and prior variance leads to an expansion of the unknown parameter space, which in turn reduces the search accuracy. However, if the parameter space is too small, there is a risk that it may not contain the true values. Therefore, in practical applications, an appropriate search range and prior variance should be selected based on the specific characteristics of the problem. These results demonstrate the robustness of the FHPDE method. Although the estimation accuracy slightly decreases under looser prior information or broader search ranges, the degradation is not of an order of magnitude. This indicates that the method still maintains reliable performance and is suitable for scenarios with uncertain prior information.

Table 5 Setting of different prior information.

Case	$\boldsymbol{P}_\mathrm{r}$	$\boldsymbol{P}_\mathrm{v}$
Case-1	$\mathcal{D}(4\ \mathrm{km}^2, 4\ \mathrm{km}^2, 4\ \mathrm{km}^2)$	$\mathcal{D}(4\ (\mathrm{m/s})^2, 4\ (\mathrm{m/s})^2, 4\ (\mathrm{m/s})^2)$
Case-2	$\mathcal{D}(16\ \mathrm{km}^2, 16\ \mathrm{km}^2, 16\ \mathrm{km}^2)$	$\mathcal{D}(16\ (\mathrm{m/s})^2, 16\ (\mathrm{m/s})^2, 16\ (\mathrm{m/s})^2)$
Case-3	$\mathcal{D}(36\ \mathrm{km}^2, 36\ \mathrm{km}^2, 36\ \mathrm{km}^2)$	$\mathcal{D}(36\ (\mathrm{m/s})^2, 36\ (\mathrm{m/s})^2, 36\ (\mathrm{m/s})^2)$
Case-4	$\mathcal{D}(64\ \mathrm{km}^2, 64\ \mathrm{km}^2, 64\ \mathrm{km}^2)$	$\mathcal{D}(64\ (\mathrm{m/s})^2, 64\ (\mathrm{m/s})^2, 64\ (\mathrm{m/s})^2)$
Case-5	$\mathcal{D}(100\ \mathrm{km}^2, 100\ \mathrm{km}^2, 100\ \mathrm{km}^2)$	$\mathcal{D}(100\ (\mathrm{m/s})^2, 100\ (\mathrm{m/s})^2, 100\ (\mathrm{m/s})^2)$
Case-6	$\mathcal{D}(200\ \mathrm{km}^2, 200\ \mathrm{km}^2, 200\ \mathrm{km}^2)$	$\mathcal{D}(200\ (\mathrm{m/s})^2, 200\ (\mathrm{m/s})^2, 200\ (\mathrm{m/s})^2)$
Case-7	$\mathcal{D}(900\ \mathrm{km}^2, 900\ \mathrm{km}^2, 900\ \mathrm{km}^2)$	$\mathcal{D}(900\ (\mathrm{m/s})^2, 900\ (\mathrm{m/s})^2, 900\ (\mathrm{m/s})^2)$

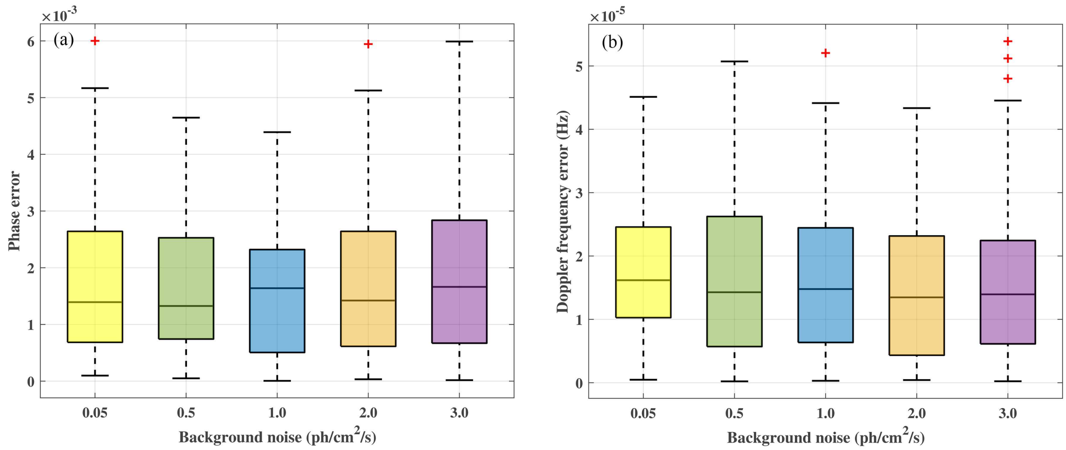

Figure 9 (Color online) Grouping box plots with different background noise. (a) Absolute value error of phase estimation; (b) absolute value error of Doppler frequency estimation.

4.5 Performance comparison of different background noise

Because the photon flux emitted by X-ray pulsars is extremely weak, background noise has a non-negligible effect on navigation accuracy. It is essential to assess the robustness of period estimation algorithms under severe noise conditions to verify their effectiveness in deep-space autonomous navigation applications. In this subsection, to examine the interference resistance of the proposed method, different background noise levels are considered, with the background noise R_b assigned values of 0.05, 0.5, 1.0, 2.0, and 3.0 ph/cm^2/s.

Figure 9(a) shows the distribution of phase estimation errors under different background noise intensities. The results indicate that as the background noise increases from 0.05 to 3.0 ph/cm^2/s, the median phase error rises slightly and the overall spread becomes wider. Nevertheless, the error level consistently remains on the order of 10^{-3}, with most samples concentrated within the interquartile range. Figure 9(b) presents the variation of Doppler shift estimation errors with respect to noise intensity. It can be observed that the median error remains largely stable within the range of 1.0×10^{-5} to 2.0×10^{-5} Hz, with only minor variations in the box and whiskers. Although the number of outliers increases under high-noise conditions, the overall distribution does not show significant deterioration. These results demonstrate that the proposed method maintains stable estimation accuracy across different noise levels and exhibits strong robustness against interference.

4.6 Performance comparison of different initial values

This subsection analyzes the sensitivity of the FHPDE method to initial values by setting different starting points. According to (57), the initial value $\boldsymbol{\theta}_0$ is set

$$\boldsymbol{\theta}_0 = \boldsymbol{\theta}_\mathrm{l} + \eta \cdot (\boldsymbol{\theta}_\mathrm{h} - \boldsymbol{\theta}_\mathrm{l}), \tag{57}$$

where $\eta \in [0, 1]$ and different initial values are obtained by adjusting η. In this study, η is set to 0, 0.1, 0.3, 0.5, 0.7, and 1, while all other simulation conditions remain consistent with Subsection 4.1. For each initial value, 100 Monte Carlo simulations are performed. The box plot of absolute errors for phase and Doppler frequency estimation under different initial values is presented in Figure 10. In Figure 10, the median of absolute errors remains stable, and the interquartile range (IQR) shows little variation, suggesting a relatively uniform error distribution. However,

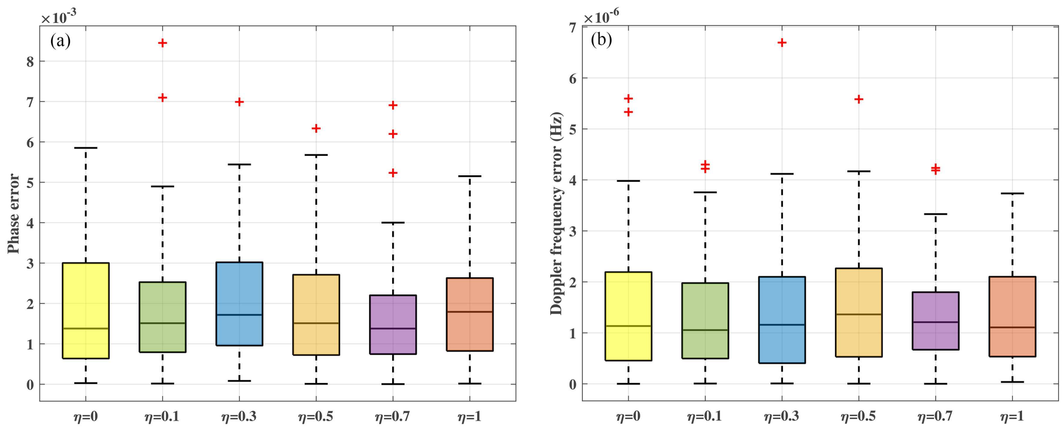

Figure 10 (Color online) Grouping box plots with different initial values. (a) Absolute value error of phase estimation; (b) absolute value error of Doppler frequency estimation.

Table 6 Details of the NICER observation data.

Obs ID	Start and end dates of observation (UTC)	Effective total observation period (s)
3013010102	2020-3-17 8:31:40–08:40:00	219.00
6013010127	2024-01-23 18:33:15–18:46:20	611.97
3013010112	2021-01-05 20:00:57–21:43:00	893.00
6013010113	2023-12-27 13:12:00–21:24:00	1179.00

outliers are observed for different initial values (such as $\eta = 0.1, 0.3$), indicating that in certain cases, the estimation error may increase.

Overall, the phase and Doppler frequency errors are relatively small and exhibit a stable distribution range, indicating that the proposed method has low sensitivity to initial values. However, further analysis is needed in future work to better address outliers.

4.7 Performance comparison of three estimation methods using NICER data

To further validate the effectiveness of the proposed method in practical missions, this subsection conducts error and time analysis using real observation data from NICER. A detailed introduction to the NICER mission can be found on NASA's website[2)]. The actual NICER observation data is available from the High Energy Astrophysics Science Archive Research Center (HEASARC)[3)]. Distinguished from the deep-space probes, NICER's low Earth orbit (LEO) operational profile provides a distinct testbed for analyzing the proposed method's adaptability to varying spacecraft operational states.

As shown in Table 6, four sets of NICER observation data with different observation times and varying observation periods are utilized in this study. The photon data released by NICER include cleaned and calibrated science events, which have undergone background noise removal, energy filtering, and good time interval (GTI) selection. However, these data have not yet been corrected to the solar system barycentric coordinate system. Therefore, in this study, the NICER data are first converted to the solar system barycenter before further analysis. The spacecraft's true state is determined using the global positioning system (GPS), with position and velocity error covariances set to $(5\ \text{km})^2$ and $(5\ \text{m/s})^2$, respectively. The true values of phase and Doppler frequency are calculated based on the actual state obtained from GPS. The pulsar's reference epoch and frequency parameters are obtained from the Jodrell Bank Centre for Astrophysics[4)]. Other pulsar parameters and estimation algorithm settings remain consistent with those in Subsection 4.1.

Analysis of the experimental results in Table 7 reveals that the FHPDE method exhibits significant advantages in both estimation accuracy and computational efficiency. Regarding estimation accuracy, the traditional MLE-Grid method shows large and unstable estimation errors due to the limitations of grid resolution. By incorporating prior information, the AGS method significantly reduces the estimation errors of phase and Doppler frequency, demonstrating the effectiveness of utilizing prior constraints to enhance estimation performance. In contrast, the

2) https://heasarc.gsfc.nasa.gov/docs/nicer/mission_guide/.
3) https://heasarc.gsfc.nasa.gov/docs/archive.html.
4) https://www.jb.man.ac.uk/pulsar/crab/crab2.txt.

Table 7 Performance comparison of three estimation methods using NICER data.

Obs ID	Method	RMSE of phase	RMSE of Doppler frequency (Hz)	GPU time (s)
3013010102	FHPDE	5.816×10^{-4}	5.401×10^{-7}	0.594
	AGS	1.412×10^{-3}	4.168×10^{-7}	0.856
	MLE-Grid	3.029×10^{-2}	1.925×10^{-5}	3348.34
6013010127	FHPDE	4.827×10^{-4}	2.181×10^{-7}	0.708
	AGS	1.474×10^{-3}	5.099×10^{-7}	0.971
	MLE-Grid	1.353×10^{-4}	7.205×10^{-6}	17226.57
3013010112	FHPDE	4.873×10^{-4}	3.964×10^{-7}	0.814
	AGS	1.420×10^{-3}	1.188×10^{-6}	1.193
	MLE-Grid	1.635×10^{-3}	1.929×10^{-6}	33121.91
6013010113	FHPDE	3.921×10^{-4}	3.771×10^{-7}	0.958
	AGS	1.161×10^{-3}	9.718×10^{-7}	1.486
	MLE-Grid	1.495×10^{-3}	1.318×10^{-6}	40323.10

FHPDE method goes a step further in phase estimation accuracy, consistently maintaining an error level at the 10^{-4} order of magnitude across all test datasets, which outperforms the AGS method while maintaining a comparable level of performance in Doppler frequency estimation.

In terms of computational efficiency, FHPDE requires minimal time, which is far lower than the tens of thousands of seconds required by the MLE-Grid method. Simultaneously, its processing speed is faster than that of the AGS method. Furthermore, as the observation duration increases from 219 to 1179 s, FHPDE maintains high execution efficiency and stability, whereas the computational burden of traditional methods grows significantly with the increase in data volume. Consequently, the FHPDE method not only surpasses existing algorithms in estimation accuracy but also possesses a substantial advantage in computational efficiency, fully demonstrating its potential for high-efficiency and high-precision X-ray pulsar-based autonomous navigation applications.

5 Conclusion and outlook

This paper proposes a fast and high-precision estimation method based on prior information and non-convex optimization to address the problem of phase and Doppler frequency shift estimation in XNAV. The performance of the proposed method has been validated through simulation experiments and NICER data analysis. The specific conclusions are as follows.

(1) Balancing real-time performance and accuracy. The FHPDE method achieves rapid convergence and, compared to traditional estimation methods, significantly improves estimation accuracy while meeting real-time requirements. This provides a superior alternative for practical XNAV missions. Additionally, the non-convex optimization approach employed in this method offers new insights and directions for researchers in related fields.

(2) Flexibility of the on-orbit phase model. Compared to existing phase models, the enhanced phase model established in this paper allows for flexible selection of reference time based on mission requirements while preserving the frequency precision of pulsars, further enhancing the model's applicability.

(3) Generality of the Bayesian risk function. By analyzing the prior statistical characteristics of the parameters to be estimated, this paper constructs a Bayesian risk function-based objective function. This model supports the incorporation of different loss functions, offering greater generality and flexibility compared to traditional single-objective functions.

Although simulation experiments demonstrate that the FHPDE method achieves rapid convergence within the constrained interval and has small errors, the method still has some limitations. Future research can focus on the following improvements.

(1) Impact of different loss functions. The Bayesian model constructed in this paper supports multiple loss functions. Future research will investigate the influence of different loss functions on the performance of the objective function to further optimize the method.

(2) Impact of outliers. Similar to many optimization algorithms, outliers appear in the estimation errors of the FHPDE method under different initial values. Outliers may lead to sub-optimal solutions or slow convergence. Future research should focus on further suppressing outliers to enhance the robustness and global convergence of the algorithm.

In summary, the FHPDE method demonstrates excellent performance in phase and Doppler frequency shift estimation for XNAV, providing a new solution for high-precision real-time navigation. Future improvements will further enhance its robustness and applicability, laying a more solid foundation for the practical application of X-ray pulsar-based navigation.

Acknowledgements This work was supported by National Natural Science Foundation of China (Grant Nos. 62373030, 42388101), Innovation Program for Quantum Science and Technology (Grant No. 2021ZD0303400), and Funds for National Key Laboratory of Inertial Measurement (Grant No. 2024-WDZC-004-08). The authors would like to extend their appreciation to all members of the Science and Technology on Inertial Laboratory, Fundamental Science on Novel Inertial Instrument and Navigation System Technology Laboratory, Institute of Large-scale Scientific Facility and Centre for Zero Magnetic Field Science, Beihang University, National Institute of Extremely-Weak Magnetic Field Infrastructure, Hangzhou, and Hefei National Laboratory, for their invaluable contributions, insights, and collaborative efforts.

References

1 Yang H, Ning X. Comment on autonomous celestial navigation technology for spacecraft. Chin J Aeronautics, 2025, 38: 103555
2 Sheikh S I, Pines D J, Ray P S, et al. Spacecraft navigation using X-ray pulsars. J Guid Control Dyn, 2006, 29: 49–63
3 Zhang W J, Ma X, Chen X, et al. X-ray pulsar navigation based on phase and Doppler frequency shift using double-differenced. IEEE Trans Instrum Meas, 2024, 73: 1–15
4 Sun H, Su J, Deng Z, et al. Grouping bi-chi-squared method for pulsar navigation experiment using observations of Rossi X-ray timing explorer. Chin J Aeronautics, 2023, 36: 386–395
5 Zhang W, Xie T, Chen X, et al. Second-differenced pulsar measurement based on phase and Doppler frequency shift for binary pulsar navigation. IEEE Trans Aerosp Electron Syst, 2025, 61: 15642–15658
6 Sala J, Urruela A, Villares X, et al. Feasibility Study for a Spacecraft Navigation System Relying on Pulsar Timing Information (Final Report). Technical Report, 2004
7 Yu W H, Semper S R, Mitchell J W, et al. NASA SEXTANT mission operations architecture. Acta Astronaut, 2020, 176: 531–541
8 Wolff M T, Guillot S, Bogdanov S, et al. NICER detection of thermal X-ray pulsations from the massive millisecond pulsars PSR J0740+6620 and PSR J1614-2230. Astrophys J Lett, 2021, 918: L26
9 Zhang X Y, Shuai P, Huang L W, et al. Mission overview and initial observation results of the X-ray pulsar navigation-i satellite. Int J Aerospace Eng, 2017, 2017: 1–7
10 Zheng S J, Ge M Y, Han D W, et al. Test of pulsar navigation with POLAR on TG-2 space station (in Chinese). Sci Sin-Phys Mech Astron, 2017, 47: 099505
11 Zheng S J, Zhang S N, Lu F J, et al. In-orbit demonstration of X-ray pulsar navigation with the insight-HXMT satellite. Astrophys J Suppl Ser, 2019, 244: 1–7
12 Sheikh S I. The use of variable celestial X-ray sources for spacecraft navigation. Dissertation for Ph.D. Degree. Maryland: University of Maryland, 2005
13 Shuai P, Li M, Chen S, et al. Principle and Method of X-ray Pulsar Navigation System. Beijing: China Astronautic Publishing House, 2009
14 Li J, Ma X, Zhang W, et al. A pulse time-delay estimation method for XNAV: nonuniformly epoch folding. IEEE Trans Aerosp Electron Syst, 2024, 60: 5577–5586
15 Wang Y, Zheng W, Zhang S, et al. Review of X-ray pulsar spacecraft autonomous navigation. Chin J Aeronautics, 2023, 36: 44–63
16 Liu G X, Li L, Lu J M, et al. Representation and solution of singular positioning issues from wireless signal intersection location technology (in Chinese). Sci Sin Inform, 2022, 52: 1992–2010
17 Liang H, Zhan Y F, Yin H L. Research on pulsars selection for X-ray pulsar navigation system. J Electron Inform Technol, 2015, 37: 2356–2362
18 Golshan A R, Sheikh S I. On pulse phase estimation and tracking of variable celestial X-ray sources. 2007. https://www.asterlabs.com/publications/2007/Golshan_&_Sheikh,_ION_63_AM_April_2007.pdf
19 Anderson K D, Pines D J, Sheikh S I. Validation of pulsar phase tracking for spacecraft navigation. J Guidance Control Dyn, 2015, 38: 1885–1897
20 Anderson K D, Pines D, Sheikh S. Investigation of X-ray pulsar signal phase tracking for spacecraft navigation. In: Proceedings of AIAA, 2022
21 Huang L W, Liang B, Zhang T. Pulse phase and Doppler frequency estimation of X-ray pulsars under conditions of spacecraft and binary motion and its application in navigation. Sci China-Phys Mech Astron, 2013, 56: 848–858
22 Xue M F, Li X P, Fu L Z, et al. X-ray pulsar-based navigation using pulse phase and Doppler frequency measurements. Sci China Inf Sci, 2015, 58: 122202
23 Wang Y, Zhang W. Pulsar phase and Doppler frequency estimation for XNAV using on-orbit epoch folding. IEEE Trans Aerosp Electron Syst, 2016, 52: 2210–2219
24 Wang Y, Zhang S, Ge M, et al. Fast on-orbit pulse phase estimation of X-ray crab pulsar for XNAV flight experiments. IEEE Trans Aerosp Electron Syst, 2023, 59: 3395–3404
25 Wang Y, Wang Y, Jiang K, et al. Adaptive grid search based pulse phase and Doppler frequency estimation for XNAV. IEEE Trans Aerosp Electron Syst, 2024, 60: 3707–3717
26 Xue M, Li X, Sun H, et al. A fast pulse phase estimation method for X-ray pulsar signals based on epoch folding. Chin J Aeronautics, 2016, 29: 746–753
27 Su J, Fang H, Bao W, et al. A maximum a posteriori estimation based method for estimating pulse time delay. Adv Space Res, 2022, 69: 3966–3982
28 Emadzadeh A A, Speyer J L. Navigation in Space by X-ray Pulsars. New York: Springer, 2011
29 Zhang H, Xu L P, Xie Q. Modeling and Doppler measurement of X-ray pulsar. Sci China-Phys Mech Astron, 2011, 54: 1068–1076
30 Wang Y S, Wang Y D, Zheng W. On-orbit pulse phase estimation based on CE-Adam algorithm. Aerospace, 2021, 8: 1–14
31 Zhang H, Xu L, Shen Y, et al. A new maximum-likelihood phase estimation method for X-ray pulsar signals. J Zhejiang Univ-Sci C, 2014, 15: 458–469
32 Chakrabarti K, Chopra N. A state-space perspective on the expedited gradient methods: Nadam, RAdam, and rescaled gradient flow. In: Proceedings of the 8th Indian Control Conference (ICC), 2022. 31–36
33 Barakat A, Bianchi P. Convergence and dynamical behavior of the ADAM algorithm for nonconvex stochastic optimization. SIAM J Optim, 2021, 31: 244–274
34 Ashby N, Golshan A R. Minimum uncertainties in position and velocity determination using X-ray photons from millisecond pulsars. In: Proceedings of the National Technical Meeting of The Institute of Navigation, San Diego, 2008. 110–118
35 Manchester R N, Hobbs G B, Teoh A, et al. The Australia Telescope National Facility pulsar catalogue. Astron J, 2005, 129: 1993–2006
36 Shuai P, Liu Q, Huang L, et al. Pulsar navigation test satellite XPNAV-1 and its observation results. J Chinese Inertial Technol, 2019, 27: 281–287

Appendix A Derivation of Eq. (8)

Eq. (7) can be expressed as

$$\phi_i^j = \phi_0^j + f_0 \left[g(t_{i,\mathrm{sc}}^j) - g(t_{0,\mathrm{sc}}^j) \right] + \frac{f_1}{2} \left\{ \left[g(t_{i,\mathrm{sc}}^j) - T_0 \right]^2 - \left[g(t_{0,\mathrm{sc}}^j) - T_0 \right]^2 \right\}. \tag{A1}$$

Let $f(\boldsymbol{r}_i^j, \boldsymbol{r}_0^j) = g(t_{i,\mathrm{sc}}^j) - g(t_{0,\mathrm{sc}}^j)$, and $h(\boldsymbol{r}_i^j, \boldsymbol{r}_0^j) = \left[g(t_{i,\mathrm{sc}}^j) - T_0 \right]^2 - \left[g(t_{0,\mathrm{sc}}^j) - T_0 \right]^2$. Then, expanding $f(\boldsymbol{r}_i^j, \boldsymbol{r}_0^j)$ and $h(\boldsymbol{r}_i^j, \boldsymbol{r}_0^j)$ around $(\hat{\boldsymbol{r}}_i^j, \hat{\boldsymbol{r}}_0^j)$ using a Taylor expansion gives

$$\begin{cases} f(\boldsymbol{r}_i^j, \boldsymbol{r}_0^j) = f(\hat{\boldsymbol{r}}_i^j, \hat{\boldsymbol{r}}_0^j) + \boldsymbol{G}_i \cdot \Delta \boldsymbol{r}_i^j - \boldsymbol{G}_0 \cdot \Delta \boldsymbol{r}_0^j, \\ h(\boldsymbol{r}_i^j, \boldsymbol{r}_0^j) = h(\hat{\boldsymbol{r}}_i^j, \hat{\boldsymbol{r}}_0^j) + 2 \left[g(\hat{t}_{i,\mathrm{sc}}) - T_0 \right] \left(\boldsymbol{G}_i \cdot \Delta \boldsymbol{r}_i^j - \boldsymbol{G}_0 \cdot \Delta \boldsymbol{r}_0^j \right). \end{cases} \tag{A2}$$

In the above, $\boldsymbol{r}_i^j = \hat{\boldsymbol{r}}_i^j + \Delta \boldsymbol{r}_i^j$, $\boldsymbol{r}_0^j = \hat{\boldsymbol{r}}_0^j + \Delta \boldsymbol{r}_0^j$. $\boldsymbol{r}_i^j$ and $\boldsymbol{r}_0^j$ represent the true positions of the spacecraft, $\hat{\boldsymbol{r}}_i^j$ and $\hat{\boldsymbol{r}}_0^j$ represent the estimated positions of the spacecraft, and $\Delta \boldsymbol{r}_i^j$ and $\Delta \boldsymbol{r}_0^j$ represent the position estimation errors of the spacecraft.

By substituting (A2) into (A1), we obtain

$$\begin{aligned} \phi_i^j &= \phi_0^j + f_0 \left[f(\hat{\boldsymbol{r}}_i^j, \hat{\boldsymbol{r}}_0^j) + \boldsymbol{G}_i \Delta \boldsymbol{r}_i^j - \boldsymbol{G}_0 \Delta \boldsymbol{r}_0^j \right] + \frac{f_1}{2} \left\{ h(\hat{\boldsymbol{r}}_i^j, \hat{\boldsymbol{r}}_0^j) + 2 \left[g(\hat{t}_{i,\mathrm{sc}}) - T_0 \right] \left(\boldsymbol{G}_i \Delta \boldsymbol{r}_i^j - \boldsymbol{G}_0 \Delta \boldsymbol{r}_0^j \right) \right\} \\ &= \phi_0^j + f_0 \cdot f(\hat{\boldsymbol{r}}_i^j, \hat{\boldsymbol{r}}_0^j) + \frac{f_1}{2} \cdot h(\hat{\boldsymbol{r}}_i^j, \hat{\boldsymbol{r}}_0^j) + \left\{ f_0 + f_1 \left[g(\hat{t}_{i,\mathrm{sc}}) - T_0 \right] \right\} \left(\boldsymbol{G}_i \Delta \boldsymbol{r}_i^j - \boldsymbol{G}_0 \Delta \boldsymbol{r}_0^j \right) \\ &= \phi_0^j + \hat{\phi}_i^j + \left\{ f_0 + f_1 \left[g(\hat{t}_{i,\mathrm{sc}}) - T_0 \right] \right\} \left(\boldsymbol{G}_i \Delta \boldsymbol{r}_i^j - \boldsymbol{G}_0 \Delta \boldsymbol{r}_0^j \right), \end{aligned} \tag{A3}$$

where $\hat{\phi}_i^j = f_0 \cdot f(\hat{\boldsymbol{r}}_i^j, \hat{\boldsymbol{r}}_0^j) + \frac{1}{2} f_1 \cdot h(\hat{\boldsymbol{r}}_i^j, \hat{\boldsymbol{r}}_0^j)$, which can be expressed as

$$\hat{\phi}_i^j = f_0 \left[g(\hat{t}_{i,\mathrm{sc}}^j) - g(\hat{t}_{0,\mathrm{sc}}^j) \right] + \frac{f_1}{2} \left\{ \left[g(\hat{t}_{i,\mathrm{sc}}^j) - T_0 \right]^2 - \left[g(\hat{t}_{0,\mathrm{sc}}^j) - T_0 \right]^2 \right\}. \tag{A4}$$

Appendix B Derivation of PCRLB

Lemma B1. Let $p(\boldsymbol{x}; \boldsymbol{\theta})$ be the probability density function of the random vector $\boldsymbol{x}$, where $\boldsymbol{\theta}$ is the unknown parameter vector. Assume that for all $\boldsymbol{\theta}$, $p(\boldsymbol{x}; \boldsymbol{\theta})$ satisfies the following "regularity" condition:

$$\mathrm{E} \left[\frac{\partial}{\partial \boldsymbol{\theta}} \ln p(\boldsymbol{x}; \boldsymbol{\theta}) \right] = 0. \tag{B1}$$

Then, for any unbiased estimator $\hat{\boldsymbol{\theta}}$, its covariance satisfies

$$\mathrm{Var} \left(\hat{\boldsymbol{\theta}} \right) \geqslant \left[I \left(\boldsymbol{\theta} \right) \right]^{-1}, \tag{B2}$$

where the inequality indicates that $\mathrm{Var} \left(\hat{\boldsymbol{\theta}} \right) - \left[I \left(\boldsymbol{\theta} \right) \right]^{-1}$ is positive semi-definite. $I \left(\boldsymbol{\theta} \right)$ represents the Fisher information, defined as

$$\left[I \left(\boldsymbol{\theta} \right) \right]_{ij} = -\mathrm{E} \left[\frac{\partial^2}{\partial \boldsymbol{\theta}_i \partial \boldsymbol{\theta}_j} \ln p(\boldsymbol{x}; \boldsymbol{\theta}) \right], \tag{B3}$$

where the partial derivatives are computed using the true value of $\boldsymbol{\theta}$, and the expectation is taken with respect to $p(\boldsymbol{x}; \boldsymbol{\theta})$. $\left[I \left(\boldsymbol{\theta} \right) \right]^{-1}$ is referred to as the CRLB.

Assume that $\boldsymbol{x} = \{ t_i^j \}_{i=0}^N$ and $\boldsymbol{\theta} = \left[\phi_0^j, f_\mathrm{d} \right]^\mathrm{T}$. Based on the established posterior objective function (31), we have

$$\ln p(\boldsymbol{\theta} | \boldsymbol{x}) = \ln p(\boldsymbol{x} | \boldsymbol{\theta}) + \ln p(\boldsymbol{\theta}). \tag{B4}$$

Thus, we obtain

$$\mathrm{E} \left[\frac{\partial \ln p(\boldsymbol{\theta} | \boldsymbol{x})}{\partial \boldsymbol{\theta}} \right] = \mathrm{E} \left[\frac{\partial \ln p(\boldsymbol{x} | \boldsymbol{\theta})}{\partial \boldsymbol{\theta}} \right] + \mathrm{E} \left[\frac{\partial \ln p(\boldsymbol{\theta})}{\partial \boldsymbol{\theta}} \right]. \tag{B5}$$

Emadzadeh et al.[5] have already proven that for all parameters, $\mathrm{E} \left[\frac{\partial \ln p(\boldsymbol{x} | \boldsymbol{\theta})}{\partial \boldsymbol{\theta}} \right] = 0$. Therefore, it is only necessary to prove that for all parameters, $\mathrm{E} \left[\frac{\partial \ln p(\boldsymbol{\theta})}{\partial \boldsymbol{\theta}} \right] = 0$.

To derive this, we take the partial derivatives of the phase and Doppler frequency, yielding the following:

$$\mathrm{E} \left[\frac{\partial \ln p(\boldsymbol{\theta})}{\partial \boldsymbol{\theta}} \right] = \mathrm{E} \left[\frac{\partial \ln p(\boldsymbol{\theta})}{\partial \phi_0^j} \right] + \mathrm{E} \left[\frac{\partial \ln p(\boldsymbol{\theta})}{\partial f_\mathrm{d}} \right]. \tag{B6}$$

5) Emadzadeh A A, Speyer J L. On modeling and pulse phase estimation of X-ray pulsars. IEEE Trans Signal Process, 2010, 58: 4484–4495.

Subsection 2.3 defines the joint probability density function for the phase and Doppler frequency, so in (B6), we have

$$\mathrm{E}\left[\frac{\partial \ln p(\boldsymbol{\theta})}{\partial \phi_0^j}\right] = \mathrm{E}\left(-\frac{1}{2(1-\rho^2)}\left[\frac{2(\phi_0^j - \tilde{\phi}_0^j)}{\sigma_{\phi_0}^2} - \frac{2\rho f_{\mathrm{d}}}{\sigma_{\phi_0}\sigma_{f_{\mathrm{d}}}}\right]\right), \tag{B7}$$

$$\mathrm{E}\left[\frac{\partial \ln p(\boldsymbol{\theta})}{\partial f_{\mathrm{d}}}\right] = \mathrm{E}\left(-\frac{1}{2(1-\rho^2)}\left[\frac{2f_{\mathrm{d}}}{\sigma_{f_{\mathrm{d}}}^2} - \frac{2\rho(\phi_0^j - \tilde{\phi}_0^j)}{\sigma_{\phi_0}\sigma_{f_{\mathrm{d}}}}\right]\right). \tag{B8}$$

Since $\mathrm{E}(\phi_0^j) = \tilde{\phi}_0^j$ and $\mathrm{E}(f_{\mathrm{d}}) = 0$, we have $\mathrm{E}\left[\frac{\partial \ln p(\boldsymbol{\theta})}{\partial \phi_0^j}\right] = 0$ and $\mathrm{E}\left[\frac{\partial \ln p(\boldsymbol{\theta})}{\partial f_{\mathrm{d}}}\right] = 0$. Therefore, $\mathrm{E}\left[\frac{\partial \ln p(\boldsymbol{\theta})}{\partial \boldsymbol{\theta}}\right] = 0$, which implies that $\mathrm{E}\left[\frac{\partial}{\partial \boldsymbol{\theta}} \ln p(\boldsymbol{x};\boldsymbol{\theta})\right] = 0$ satisfies the "regularity" condition.

Based on (B3) and (B4), the Fisher information is expressed as

$$[I(\boldsymbol{\theta})]_{ij} = -\mathrm{E}\left(\frac{\partial^2 \ln p(\boldsymbol{\theta}|\boldsymbol{x})}{\partial \boldsymbol{\theta}_i \partial \boldsymbol{\theta}_j}\right) = -\mathrm{E}\left[\frac{\partial^2 \ln p(\boldsymbol{x}|\boldsymbol{\theta})}{\partial \boldsymbol{\theta}_i \partial \boldsymbol{\theta}_j}\right] - \mathrm{E}\left[\frac{\partial^2 \ln p(\boldsymbol{\theta})}{\partial \boldsymbol{\theta}_i \partial \boldsymbol{\theta}_j}\right], \tag{B9}$$

where $i, j = 1, 2$, $\boldsymbol{\theta}_1 = \phi_0^j$ and $\boldsymbol{\theta}_2 = f_{\mathrm{d}}$. Let the first term on the right-hand side of (B9) be denoted as I_x and the second term as I_θ. Thus, we have $I(\boldsymbol{\theta}) = I_x + I_\theta$. Emadzadeh et al.[5)] provided the expression for I_x as

$$I_x = \frac{L}{6}\begin{bmatrix} 6T_{\mathrm{obs}} & 3T_{\mathrm{obs}}^2 \\ 3T_{\mathrm{obs}}^2 & 2T_{\mathrm{obs}}^3 \end{bmatrix}, \tag{B10}$$

where

$$L = \int_0^1 \frac{[\lambda_s h'(\phi)]^2}{\lambda_b + \lambda_s h(\phi)} \mathrm{d}\phi. \tag{B11}$$

From (B7) and (B8), I_θ is given by

$$I_\theta = \begin{bmatrix} \frac{1}{(1-\rho^2)\sigma_{\phi_0}^2} & -\frac{\rho}{(1-\rho^2)\sigma_{\phi_0}\sigma_{f_{\mathrm{d}}}} \\ -\frac{\rho}{(1-\rho^2)\sigma_{\phi_0}\sigma_{f_{\mathrm{d}}}} & \frac{1}{(1-\rho^2)\sigma_{f_{\mathrm{d}}}^2} \end{bmatrix}. \tag{B12}$$

Therefore, the Fisher information is expressed as

$$I(\boldsymbol{\theta}) = \begin{bmatrix} I_{11} & I_{12} \\ I_{21} & I_{22} \end{bmatrix} = \begin{bmatrix} LT_{\mathrm{obs}} + \frac{1}{(1-\rho^2)\sigma_{\phi_0}^2} & \frac{LT_{\mathrm{obs}}^2}{2} - \frac{\rho}{(1-\rho^2)\sigma_{\phi_0}\sigma_{f_{\mathrm{d}}}} \\ \frac{LT_{\mathrm{obs}}^2}{2} - \frac{\rho}{(1-\rho^2)\sigma_{\phi_0}\sigma_{f_{\mathrm{d}}}} & \frac{LT_{\mathrm{obs}}^3}{3} + \frac{1}{(1-\rho^2)\sigma_{f_{\mathrm{d}}}^2} \end{bmatrix}. \tag{B13}$$

Since $I(\boldsymbol{\theta})$ is a diagonal matrix, according to Lemma B1, the PCRLB is given by

$$\mathrm{PCRLB}\left(\hat{\phi}_0^j, \hat{f}_{\mathrm{d}}\right) = [I(\boldsymbol{\theta})]^{-1} = \frac{1}{\Delta}\begin{bmatrix} I_{22} & -I_{12} \\ -I_{21} & I_{11} \end{bmatrix}, \tag{B14}$$

where Δ is a constant related to the pulsar and navigation parameters and is given by

$$\Delta = I_{11}I_{22} - I_{12}^2 = L^2T_{\mathrm{obs}}^4(1-\rho^2)\sigma_{\phi_0}^2\sigma_{f_{\mathrm{d}}}^2 + 12\sigma_{\phi_0}^2 LT_{\mathrm{obs}} + 4\sigma_{f_{\mathrm{d}}}^2 LT_{\mathrm{obs}}^3 + 12\rho\sigma_{\phi_0}\sigma_{f_{\mathrm{d}}} LT_{\mathrm{obs}} + 12 > 0. \tag{B15}$$

Therefore,

$$\begin{cases} \mathrm{PCRLB}\left(\hat{\phi}_0^j\right) = \frac{4LT_{\mathrm{obs}}^3(1-\rho^2)\sigma_{f_{\mathrm{d}}}^2 + 12}{\Delta} \cdot \sigma_{\phi_0}^2, \\ \mathrm{PCRLB}\left(\hat{f}_{\mathrm{d}}\right) = \frac{12LT_{\mathrm{obs}}(1-\rho^2)\sigma_{\phi_0}^2 + 12}{\Delta} \cdot \sigma_{f_{\mathrm{d}}}^2. \end{cases} \tag{B16}$$